

# **UNDERSTANDING OF MUTUAL INTERACTIONS BETWEEN LIQUID JETS: ENTRAINMENT AND SHEET FORMATION**

## **A REPORT**

*Submitted in partial fulfillment of the  
requirements for the award of the degree  
of*

**MASTER OF TECHNOLOGY**  
in  
**MECHANICAL ENGINEERING**  
(With Specialization in Thermal Engineering)

*By*

**VATSAL SANJAY**



**DEPARTMENT OF MECHANICAL AND INDUSTRIAL ENGINEERING  
INDIAN INSTITUTE OF TECHNOLOGY ROORKEE  
ROORKEE - 247 667 (INDIA)  
NOVEMBER, 2017**

## **CANDIDATE'S DECLARATION**

I, VATSAL SANJAY, hereby certify that the work which is being presented in the report entitled "**UNDERSTANDING OF MUTUAL INTERACTIONS BETWEEN LIQUID JETS: ENTRAINMENT AND SHEET FORMATION**" in partial fulfillment of the requirements for the award of the degree of "MASTER OF TECHNOLOGY" in Mechanical Engineering with specialization in Thermal Engineering, submitted to the Department of Mechanical and Industrial Engineering of the Indian Institute of Technology Roorkee is an authentic record of my own work carried out during the period from January, 2017 to November, 2017 under the supervision of Dr. Arup Kumar Das, Assistant Professor, Department of Mechanical and Industrial Engineering, Indian Institute of Technology Roorkee.

I have not submitted the matter embodied in this report for the award of any other degree or diploma.

Date: November 14, 2017

Place: Roorkee

**(VATSAL SANJAY)**

---

## **CERTIFICATION**

This is to certify that the above statement made by the candidate is correct to the best of my knowledge and belief.

**(Dr. ARUP KUMAR DAS)**  
Assistant Professor, Department of  
Mechanical and Industrial Engineering  
Indian Institute of Technology  
Roorkee, Uttarakhand - 247667, India

## Abstract

Formation of liquid chain is studied through a series of fully resolved detailed numerical simulations. The collision of liquid jets and formation of a sheet in the median plane is illustrated numerically. The sheet subsequently transforms into a chain like fluidic structure with successive dwarf links in mutually orthogonal planes. This structure is analyzed to pertain towards a steady state. Since the velocity of the sheet is super-critical (higher than the speed of the capillary waves), the first link is studied for the flow kinematics. To understand the behavior of fluid parcels inside the chain, flow is studied with streamlines. Their radial dispatch after the collision of jets is followed by self-similar paths with respect to the chain outer periphery. Further, a scaled law is presented for the variation of fluid velocity across the azimuthal direction of the flow. The influence of several non-dimensional parameters has been found on the first link of the chain. This has been generalized over the entire chain structure. For the understanding of chain profiles over a wide range of operating parameters, a correlation has been proposed based on numerical simulations and subsequent regression analysis. Citing analogy between the impact of jets for the formation of elemental links and traversal of non-deformable fluid quanta after the collision, an attempt has been made to understand the fundamental physics of this phenomenon through force balance. The analogy helps to take into account the role of surface tension and other forces on the shape and size of the liquid sheets. Further, the formation of higher order links is proposed as equivalent to the collision between the liquid rims bounding the sheet, modeled as the jets of reduced strengths and smaller impingement angles. Finally, we assess the effects of various fluid properties on the dimensions of these links, illustrating the viscous dissipation at the time of collisions.

# Contents

<b>CANDIDATE'S DECLARATION</b>	<b>i</b>
<b>Abstract</b>	<b>ii</b>
<b>List of Figures</b>	<b>iv</b>
<b>List of Tables</b>	<b>vi</b>
<b>1 Introduction</b>	<b>1</b>
1.1 Motivation and background . . . . .	2
1.2 Literature Survey . . . . .	2
1.3 Lacuna in literature . . . . .	3
1.4 Objectives of the present work . . . . .	4
1.5 Organization of the report . . . . .	5
<b>2 Numerical Framework</b>	<b>6</b>
2.1 Introduction . . . . .	7
2.2 Governing equations . . . . .	7
2.3 Process parameters and mesh sensitivity analysis . . . . .	8
2.4 Validation of the numerical model . . . . .	9
<b>3 Collision of liquid jets</b>	<b>11</b>
3.1 Collision and Sheet formation . . . . .	12
3.1.1 The process of chain formation . . . . .	12
3.1.2 Velocity variation inside the sheet . . . . .	12
3.1.3 Three dimensional streamline structure . . . . .	15
3.2 Parametric Variation . . . . .	16
3.2.1 Variation of control parameters . . . . .	17
3.2.2 Prediction of chain structure using regression analysis . . . . .	18
3.3 Analytical Model . . . . .	19
3.4 Inter-relation between inter-connected links . . . . .	22
<b>4 Conclusion and Future Work</b>	<b>25</b>
4.1 Conclusion . . . . .	26
4.2 Future Work . . . . .	26
<b>Achievements till date</b>	<b>27</b>
<b>References</b>	<b>28</b>

# List of Figures

1.1	Formation of the liquid sheet by the collision of laminar jets. (a) Different structural features and length scales. (b) The primary link structure colored based on half times the magnitude of the sheet thickness, non-dimensionalized with the jet diameter $(\frac{h}{2d_j})$ . . . . .	4
2.1	(a) Mesh sensitivity analysis for a representative chain structure with the outer periphery and velocity profile near the inlet and (b) representation of the Adaptive Mesh Refinement (AMR) technique at critical locations. . . . .	9
2.2	Illustration of the validation of numerical model undertaken by comparison of (a) numerical interface and (b) liquid flux variation with the azimuthal angle, $\theta$ . The numerically obtained results are superimposed with the respective experimental values obtained by Bush and Hasha, 2004. . . . .	10
3.1	Formation of the liquid chain due to the collision of laminar jets. The figure illustrates the transient period through the temporal advancement from (a) pre-collision symmetric jets to $T(\frac{u_j t}{d_j}) =$ (b) 1.5, (c) 4, (d) 5, (e) 5.5, (f) 6.5, (g) 8.5, (h) 14.5, (i) 18.5 and (j) 20. The variation of $d_1$ and $l_1$ with time is shown in inset ( $\alpha, Fr, Re/Fr, Bo = 30^\circ, 2.5, 34, 5$ ). The video for this figure is added as a supplementary material. . . . .	13
3.2	Flow kinematics of the fluid parcels: (a) velocity vector field for two representative cases, (b) variation of velocity in the radial direction for four representative cases and (c) their radially averaged sheet velocity ( $u_s(\theta)$ ), non-dimensionalized with the average sheet velocity ( $u_0$ ) along the azimuthal direction in the sheet. The parameters identifying the identity of the cases follow ( $\alpha, Fr, Re/Fr, Bo$ ). . . . .	14
3.3	Three dimensional velocity field for ( $\alpha, Fr, Re/Fr, Bo$ ) = ( $30^\circ, 2, 1125, 3.4$ ) with (a) XY plane streamlines, (b) velocity vector field in the YZ plane at different collision locations, (c) the three dimensional stable chain structure, (d) streamlines at maximum link widths in the YZ plane and (e) XZ plane streamlines. . . . .	15
3.4	Three dimensional streamlines embedded on the chain structure illustrating the twist incurred as they traverse through the region of subsequent collisions for $\alpha = 30^\circ, Fr = 2, Bo = 3.4$ and (a) $Re/Fr = 1750$ and (b) $Re/Fr = 34$ . The figures in inset show the offset ( $\delta y$ from XZ plane and $\delta z$ from XY plane) of the streamline at the extreme end of the chain structure as it moves downstream with the flow for the corresponding cases. . . . .	16
3.5	Variation of first link boundary with (a) $\alpha$ at $Fr = 2.5, Bo = 4.57$ and $Re/Fr = 34$ (b) $Fr$ at $\alpha = 30^\circ, Bo = 3.4$ and $Re/Fr = 34$ (c) $Bo$ at $\alpha = 30^\circ, Fr = 2.5$ and $Re/Fr = 34$ and (d) $Re/Fr$ at $\alpha = 30^\circ, Fr = 2$ and $Bo = 3.4$ . . . . .	17
3.6	High fidelity numerical simulations of liquid jets collision to form chain structure for variation of (a) $\alpha$ at $Fr = 2.5, Bo = 4.57$ and $Re/Fr = 34$ (b) $Fr$ at $\alpha = 30^\circ, Bo = 3.4$ and $Re/Fr = 34$ (c) $Bo$ at $\alpha = 30^\circ, Fr = 2.5$ and $Re/Fr = 34$ and (d) $Re/Fr$ at $\alpha = 30^\circ, Fr = 2$ and $Bo = 3.4$ . . . . .	18

3.7 Comparison between the values of expansion of the sheet outer periphery ( $\Delta Z(x)$ ) as predicted from equation 3.5 and from numerical simulations for different test cases with (symbol, $\alpha$ , $Fr$ , $Bo$ , $Re/Fr$ ) = (■, $30^\circ$ , 2.5, 5, 34); (+, $30^\circ$ , 2.5, 4, 34); (◆, $30^\circ$ , 2.5, 2.3, 20); (×, $25^\circ$ , 2.5, 4.57, 34) and (●, $30^\circ$ , 2.5, 3.75, 20). The first two inset figures (from the left) visualizes the corresponding three dimensional structure of the first link for the primary link and the third inset depicts the comparison between the equation 3.5 and the results of Bush and Hasha, 2004. . . . .	19
3.8 Fluid quanta collision analogy: (a) schematic of the model and free-body diagram and comparison between the link shape obtained through numerical simulations and the fluid quantum trajectory ( $\zeta$ , ■) for $(\alpha, Fr, Re/Fr, Bo) = (a) (30^\circ, 2.5, 34, 5), (b) (30^\circ, 2.5, 23, 3.85), (d) (30^\circ, 2, 34, 4.56)$ and (e) $(45^\circ, 2, 34, 3.4)$ . . . . .	20
3.9 Inter-relation between links of chain reproduction of secondary link of Case 1 ( $\alpha = 30^\circ$ , $Fr = 2.5$ , $Bo = 4$ , $Re/Fr = 34$ ) as primary link of case 2 ( $\alpha = 25^\circ$ , $Fr = 2.2$ , $Bo = 4$ , $Re/Fr = 34$ ) and tertiary link of Case 1 as secondary link of Case 2 and primary link of case 3 ( $\alpha = 11.25^\circ$ , $Fr = 1.98$ , $Bo = 4$ , $Re/Fr = 34$ ) using (a) three dimensional chain structure and (b) two dimensional planar link locations. . . . .	21
3.10 Generalization of fluid rim collision for the higher order links with the prediction of angles of impingement for (a) secondary and (b) tertiary collisions and (c) the account of rim strength ( $Fr$ ) in different links. . . . .	22
3.11 Evaluation of the dimensional characteristics of the secondary and tertiary links relative to the primary link, for variations of (a) $\alpha$ at $Fr = 2.5$ , $Bo = 4.57$ and $Re/Fr = 34$ (b) $Fr$ at $\alpha = 30^\circ$ , $Bo = 3.4$ and $Re/Fr = 34$ (c) $Bo$ at $\alpha = 30^\circ$ , $Fr = 2.5$ and $Re/Fr = 34$ and (d) $Re/Fr$ at $\alpha = 30^\circ$ , $Fr = 2$ and $Bo = 3.4$ . . . . .	23

# List of Tables

2.1	Performance data of the processors used for simulations to determine the refinement level in the Grid Independence Study. The simulations are done using four Intel Core i7-6500U CPU having clock speed of 2.5GHz each and 8 GB RAM. . . . .	9
3.1	Factors ( $C_{m,n}$ ) involved in equation 3.6 determined by linear regression analysis to find the polynomial coefficients of equation 3.5. . . . .	19
4.1	Work Plan . . . . .	26

# **Chapter 1**

# **Introduction**

## 1.1 Motivation and background

Interactions of liquid jets have invoked the curiosity of researchers with their ubiquitous presence, eminent even in the scientific artworks by Da Vinci, 1508. The theoretical and experimental analysis accounting for different types of interactions involving liquid jets is classically summarized in a recent effort by Eggers and Villermaux, 2008. Most elemental among these interactions is the collision between liquid jets which is one of the canonical configurations for generation of liquid sheets. This gives way to atomized droplets in high inertial regime. If the strengths of the two jets are identical, the liquid sheet is formed in the median plane, ie., mid-way between the jets at the point of collision. (Bush and Hasha, 2004). This configuration is usually employed in the afterburners of the aircraft or in the thrust engines used in rockets (Chen et al., 2013) and has advantages over the conventional coaxial liquid-gas jet atomization technique because of the improved inertial driven destabilization and mixing between jets (Erni and Elabbadi, 2013). Moreover, the droplets formed in this process come from the thin sheet, making the droplet size distribution skewed towards the lower size and more evenly spread (Inoue et al., 2008, 2009) as compared to the droplets formed from the single jet atomization as the latter are ejected from a thick liquid jet core instead of a thin sheet. This aids in the post-atomization combustion process (Lhuissier and Villermaux, 2011). The collision of laminar jets to form stable sheets is the fundamental case of such atomization processes and also holds physical significance for the exploration of physics behind atomization. Moreover, these structures can be used as wall-free continuous reactors (Erni and Elabbadi, 2013) as well. At low velocities or narrow angles of impingement, jets may coalesce to form a unified one or they may bounce off due to the presence of a thin film of air between them (Wadhwa et al., 2013). On increasing the flow rates, laminar jets may lead to the formation of a stable liquid sheet bounded by the thicker rims at the periphery (Yang et al., 2014). The inertial and the gravitational forces act to expand the liquid sheet formed, but the action of surface tension helps the sheet to converge so that the successive collisions of the thick rims downstream of the flow result in the formation of mutually orthogonal liquid sheets (Bush and Hasha, 2004). Figure 1.1(a) illustrates this structure termed as the liquid chain with the complementary orthogonal sheets forming the different links.

## 1.2 Literature Survey

Rayleigh, 1879, 1889 was probably the first researcher to formally study the chain like structures. He reported that the chain structure was generated because of the undulations formed at the surface of a single elliptical liquid jet. Unlike cylindrical jets, they do not have an axis of overall symmetry. This results in thickening of the jet at the periphery leading to the formation of the chain like structure due to collision of these rims.

Taylor, 1960 formulated an impingement theory for impact of liquid jets to form a fluid sheet at the median plane, mid-way between the jets. Prior to his work, only the inertial and gravitational forces were considered to describe the phenomenon which gave an expanding liquid sheet. He realized that the flow inside the thicker rim at the periphery can be sustained only if the surface tension force provides the necessary centripetal acceleration to the fluid parcels inside the rim. The velocity field in the rim is also accelerating due to loss of gravitational potential. On balancing the inertial and surface tension forces, Taylor, 1960 proposed an expression for the sheet radius, given by  $r_{max} = \rho u_0 Q(\theta)/(2\sigma)$  (where,  $u_0$  denotes the average sheet velocity assumed constant throughout including the rim,  $Q(\theta)$  implies liquid flux distribution inside the sheet and  $\rho, \sigma$  are the fluid density and its surface tension coefficient with the air respectively).

Bush and Hasha, 2004 worked on the classical formulation proposed by Taylor, 1960 and gave a comprehensive theoretical and experimental theory for collision of liquid jets. They introduced several regimes to characterize the different flow structures obtained from such collisions and gave an exhaustive experimental analysis of the stable liquid chain formed by the collision of laminar jets. Their work also verifies the formulation given by Taylor, 1960 which predicts the sheet dimensions within experimental precision. Emphasis has been also given by Bush and Hasha, 2004 for prediction of shapes of leaf-like

links forming chain structure. We have used the results developed by them to validate our numerical model.

Ibrahim and Przekwas, 1991 demonstrated that the stable sheet structures can serve as the base case for the atomization studies because the droplets are formed from the perturbed liquid sheet. At high viscosities, different flow instabilities die down but at higher inertial strengths, as the flow becomes turbulent, the flapping atomization takes place.

Bremond and Villermaux, 2006 studied the several instabilities modes related to the rim at the periphery of the sheet. These instabilities are magnified as the velocity of fluid parcels inside the rims increase and the curvature dependent surface tension forces are not able to maintain equilibrium. First, finger like projections are observed at the rims' outer boundaries causing Plateau-Rayleigh instability and droplet generation.

Clanet and Villermaux, 2002; Villermaux and Clanet, 2002 discussed the instabilities inside the liquid sheet. As the velocity exceeds a critical value, the Kelvin-Helmholtz instability takes over and results in formation of destabilizing waves. This also speeds up the process of fingering instabilities at the peripheral rim of the sheet.

Choo and Kang, 2001, 2002, 2007 have worked extensively on the characterization of the first link of the chain structure, including the velocity field inside. Contrary to the earlier belief, they have shown that the sheet velocity is not a constant parameter but varies with the azimuthal angle variation. This has been demonstrated in our studies as well. Moreover, they have also discussed the variation in the sheet characteristics with respect to the velocity profile at the exit of the nozzles, inside the jets. They prescribe a parabolic profile gives a better estimate for the fully developed laminar jet as compared to the uniform profile or any other power law fit. Further, they gave the justification for the presence of thicker liquid rim at the periphery using Particle Image Velocimetry (PIV) technique. The radial streamlines were observed near the point of impingement and the fluid parcels travel towards the periphery resulting in the formation of the thick rim due to fluid accumulation.

Inamura and Shirota, 2014 studied the presence of stagnation point inside the liquid sheet. Unlike the head on collision of liquid jets where this point is at the point of intersection of the jets, it was found to shift upstream by some factor. The factor was found to be dependent on the impingement angle. These works summarize the variation of fluid velocity inside the sheet.

Yang et al., 2014 discussed the influence of different flow parameters on the shape and size of the first link in the chain structure. They acknowledged the variations due to physical parameters as well. In the present study, their arguments are generalized for the entire chain structure.

Chen et al., 2013 have shown the formation of liquid chain using Finite Volume based Volume of Fluid (VOF) framework. They attempted the reproduction of different flow regimes as proposed by Bush and Hasha, 2004. The same numerical framework is used in the present method with some modifications on the mesh refinement criteria.

Da et al., 2016 also demonstrated the formation of liquid chain using Boundary Element Method (BEM). This simulation work comprises of inviscid flow assumption but gives mesmerizing fluid structures. They have successfully reproduced all the regimes observed in the experimental works but fail to acknowledge the internal dynamics of the liquid sheet.

### 1.3 Lacuna in literature

Critical assessment of literature reveals that an in-depth study of fluid chain regime is still due which can explore fundamental physics behind the formation of primary link and establish a relation between successive diminishing links. Moreover, most of the analytical or empirical models used to describe the flow need input from the experiments to close the system of equations prior to obtaining any solution (Bush and Hasha, 2004). Moreover, the work in the direction of numerical simulation to obtain such structures is few as per the knowledge of the author (Chen et al., 2013; Da et al., 2016). A major challenge that lies in the prediction of the chain-like structure is the proper resolution of the sheet (approximately

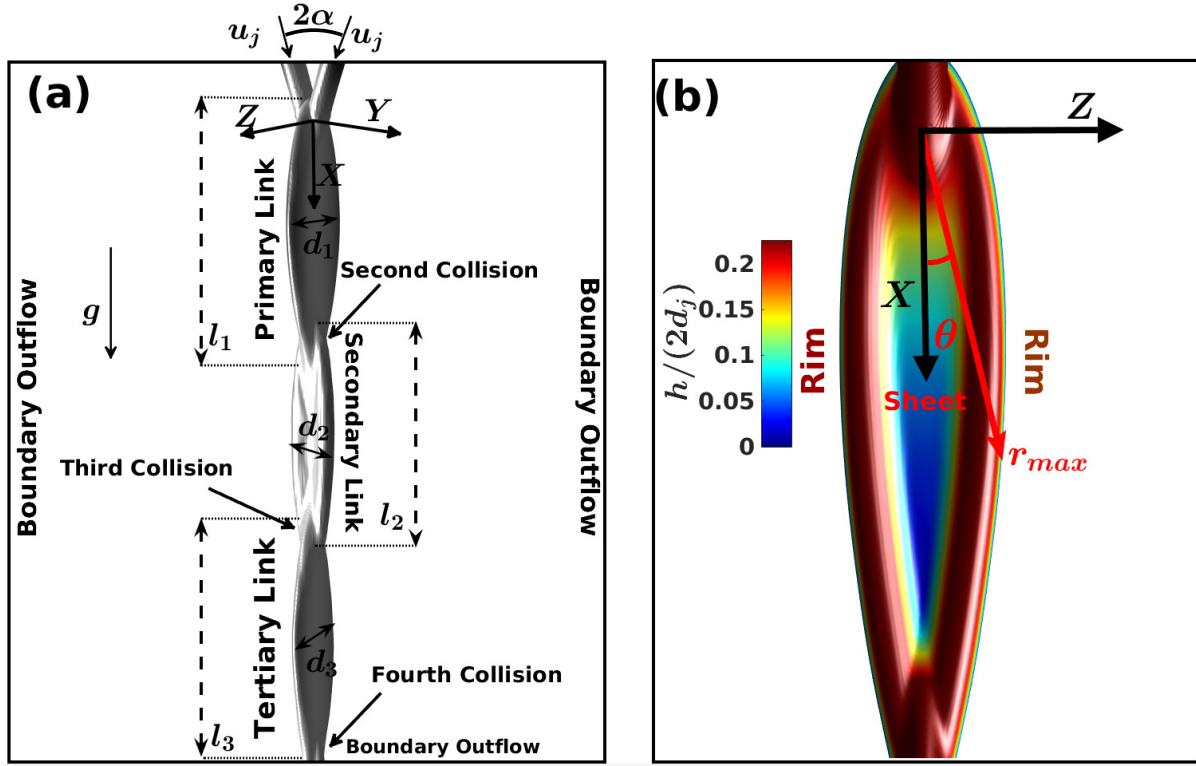


FIGURE 1.1: Formation of the liquid sheet by the collision of laminar jets. (a) Different structural features and length scales. (b) The primary link structure colored based on half times the magnitude of the sheet thickness, non-dimensionalized with the jet diameter  $\left(\frac{h}{2d_j}\right)$ .

$1/100^{th}$  of jet diameter) between the rims, which are supposed to mingle once again for forming next link in a mutually perpendicular plane. Figure 1.1(b) demonstrates the presence of a diversity of length scales in such a simplistic fluid link. If the grid resolution is not sufficient, occurrence of numerical pinch-off is observed, whereby non-physical holes are created inside the sheet because of the lack of cells. The works of Da et al., 2016 do give satisfactorily result in this regard but, their exhibition of chain-like structure along with other physical jet related structures is limited to inviscid fluids. The inability of their numerical model to incorporate viscosity has led to inaccuracies in the study of chain structure along with its kinematics and dynamics.

## 1.4 Objectives of the present work

- To understand the formation of fluid chain through a series of temporal snapshots leading to the formation of a steady structure after initial transients.
- To study the overall behavior of the fluid chain while focusing on the physics of flow for the primary link by analyzing the dimensional characteristics and velocity fields.
- To generalize the overall behavior of the fluid chain structure from the characteristics of the first link.
- To model the collision of liquid jets in a manner analogous to the impact of discrete non-deformable fluid parcels (hereinafter referred as fluid quanta or particles).
- To analyze the formation of higher order links as a result of the collision of rims of the preceding links.

## 1.5 Organization of the report

The current work is undertaken to understand the fundamental physics behind the formation of the liquid chain structure. The present chapter summarizes the work done so far in this regard. The following chapter includes the description of the mathematical model used to simulate the collision of liquid jets. In chapter 3 represents the results of the present study. At first, a series of transient features are studied to reach a steady state structure. We have Special attention is given to the second and third collisions, leading to the formation of the subsequent mutually orthogonal links. The flow kinematics are studied based on the velocity field inside the sheet. The impact of fluid quanta is then used to model the behavior of fluid parcels inside the sheet. Post-collision, the effect of surface and viscous forces is included with a constant magnitude force, which is always perpendicular to the trajectory of individual fluid quantum. This helps to understand the dynamics of liquid sheet formation. The second important aspect of our work is to generalize the impingement model for the entire chain structure, taking into account the reduced strength of rims that collide to form the subsequent perpendicular links.

## **Chapter 2**

# **Numerical Framework**

## 2.1 Introduction

The collision of liquid jets has been studied in three-dimensional finite volume framework. Open source freeware, transient, multi-fluid, Navier-Stokes solver Gerris is used for the current study. Developed by Popinet, 2003, 2009, Gerris has provided a stable and accurate platform for surface tension inclusive flows. It has been successful used frequently by researchers, such as Chen et al., 2013; Kumar et al., 2016, 2017a,b, to delve into similar problems in interfacial flows involving liquid sheets, jet and thin features like ligaments and films to capture intricate flow details and investigate the process. In this chapter, the detailed numerical framework adopted by Gerris is given. First, the governing equations and the corresponding discretization schemes are discussed followed by an illustration of the adaptive mesh refinement and grid independence study. At the end, a brief description about the work to validate the numerical model is presented.

## 2.2 Governing equations

Conventional mass and momentum conservation equations for incompressible flow have been solved in presence of the surface tension and gravitational force. Equation 2.1 contains the mass conservation equation for incompressible flow, which simply states that the velocity field ( $V_i = V_1 \hat{i} + V_2 \hat{j} + V_3 \hat{k}$ ) must be divergence free.

$$\frac{\partial V_i}{\partial x_i} = 0 \quad (2.1)$$

The momentum equation for the incompressible Newtonian fluids that is solved for all the spatial coordinates can be summarized as given in equation 2.2. In the equation, the forces applied on the control volume chosen consist of the pressure in form of its gradient  $\left(\frac{\partial P}{\partial x_i}\right)$ , the volume specific body force due to gravitation ( $\rho g_i$ ), the surface forces due to shear stress ( $2\mu D_{i,k}$ , where  $\mu$  represents the coefficient of dynamic viscosity and  $D_{i,k}$  is the deformation tensor) and the interface specific surface tension force ( $\sigma \kappa$ , where  $\sigma$  is the surface tension coefficient and  $\kappa$  denotes the curvature of the interface).

$$\rho \left( \frac{\partial V_i}{\partial t} + V_k \frac{\partial V_i}{\partial x_k} \right) = - \frac{\partial P}{\partial x_i} + \frac{\partial (2\mu D_{i,k})}{\partial x_k} + \sigma \kappa \delta_s m_i + \rho g_i \quad (2.2)$$

Moreover, the surface tension term is multiplied with the Dirac distribution function ( $\delta_s$ ) to ensure that the force due to surface tension acts only at the interface having a normal vector  $m_i$ . Further, the deformation tensor  $D_{i,k}$  is defined using the symmetric part of the velocity field gradient as given in equation 2.3.

$$D_{i,k} = \frac{1}{2} \left( \frac{\partial V_i}{\partial x_k} + \frac{\partial V_k}{\partial x_i} \right) \quad (2.3)$$

The equation 2.2 implicitly takes care of the mechanical energy. Moreover, the temperature variations are too small to affect the phenomenon being investigated and therefore, no thermal energy equation is considered. The interface tracking is done using the Volume Of Fluid (VOF), a front capturing approach involving volume fraction of liquid, defined as  $\Psi(x_i, t)$ , at the spatial and temporal instance of  $x_i$  and  $t$  respectively. The density and viscosity for the study can be described using equation 2.4 in terms of a generic property  $A$ .

$$A(\Psi) = \Psi A_1 + (1 - \Psi) A_2 \quad \forall A \in \{\rho, \mu\} \quad (2.4)$$

The VOF approach is implemented in a two-step process of interface reconstruction (based on the values of  $\Psi$  and piecewise linear interface construction scheme, PLIC) along with geometric flux computation and interface advection, shown in equation 2.5.

$$\frac{\partial \Psi}{\partial t} + \frac{\partial (\Psi V_i)}{\partial X_i} = 0 \quad (2.5)$$

Gerris uses second-order accurate time discretization of momentum and continuity equations with time splitting algorithm as proposed by Chorin, 1968, whereby an unconditionally stable corrector predictor time marching approach is adopted. A multigrid solver is used for the solution of the resulting pressure-velocity coupled Laplace equation. The advection term of the momentum equation ( $V_k \frac{\partial V_i}{\partial X_k}$ ) is estimated using the Bell-Colella-Glaz second-order unsplit upwind scheme (Bell et al., 1989), which requires the restriction to be set up on the time step. Following Popinet, 2009, time step has been determined to satisfy Courant-Friedrich-Lowy (CFL) stability criteria of less than unity. The details of solution procedure can be found in the works of Popinet, 2003, 2009. In the next section, we have looked at the different process parameters which are relevant to this study followed by a grid independence study of the results.

## 2.3 Process parameters and mesh sensitivity analysis

The computational domain is also illustrated in figure 1.1(a) with parabolic inflow (equation 2.6 as suggested by Choo and Kang, 2007) of jets (diameter,  $d_j$  and impingement angle,  $2\alpha$ ) and boundary outflow elsewhere. In equation 2.6,  $u_n$  is the inlet velocity,  $u_j$  is the average velocity,  $r$  is the radial location in the jet from its centerline and  $d_j$  is the jet diameter.

$$\frac{u_n}{u_j} = 2 \left( 1 - \left( \frac{2r}{d_j} \right)^2 \right) \quad (2.6)$$

Following equations 2.1 to 2.6, one can easily see that the different features of the liquid sheets can be represented in terms of the kinematic and dynamic properties, such as jet velocity ( $u_j$ ), its diameter ( $d_j$ ), angle of impingement ( $2\alpha$ ), acceleration due to gravity ( $g$ ) and other physical properties such as the density of the fluid ( $\rho$ ), its viscosity ( $\mu$ ) and the coefficient of surface tension ( $\sigma$ ) at the fluid-air interface.

On performing non-dimensional analysis, it can be observed that Froude number ( $Fr = \frac{u_j}{\sqrt{gd_j}}$ ), Bond number ( $Bo = \frac{\rho g d_j^2}{\sigma}$ ) and ratio between Reynolds number and jet Froude number ( $Re/Fr = \frac{\rho \sqrt{gd_j^3}}{\mu}$ ) govern the shape and sizes of different links in the fluid chain structure.

The spatial discretization of the domain is undertaken using an octree-based structured hierarchical grid system, locally refined near the interface. It is necessary to capture the smallest features of the flow, in this case, the thickness of the liquid sheet. The multi-level grid structure adapts itself according to the gradient of the tracer  $\Phi$ , which implies that the structured octree mesh is finest at the interface between the two fluids. Choo and Kang, 2001; Hasson and Peck, 1964 have shown that the thickness of the liquid sheet can be given by the equation 2.7. This expression has been found to describe the thickness of the liquid sheet within experimental precision by several independent researchers (Choo and Kang, 2001; Ekimova et al., 2015; Shen and Poulikakos, 1998).

$$\frac{hr}{d_j^2} = \frac{1}{4} \frac{\sin^2 \alpha}{(1 - \cos \theta \cos \alpha)^2} \quad (2.7)$$

Here,  $r$  is the radial direction originating from the collision point of the jets and  $h$  is the measurement of the thickness of the film produced. Even though minima of equation 2.7 occurs at  $\theta \rightarrow \pi$ , it must be noted that the decrement in thickness is more prominent because of the increase in radial distance downstream of the first collision point ( $h \propto \frac{1}{r}$ ). Further, it can also be shown that the thickness of liquid sheet follows  $\frac{hr}{d_j^2} \sim 1$ , for  $2\alpha \in \{0, \pi/2\}$ . We maintained  $\frac{d_j}{\delta l} \sim 10 \frac{r_{max}}{d_j}$  to choose minimum cell size ( $\delta l$ ) and perform Grid Independence Study (GIS). The factor of 10 is included to have at least 10 grid points (Ling et al., 2015) across the smallest length scale for the structure to avoid breakage of sheet

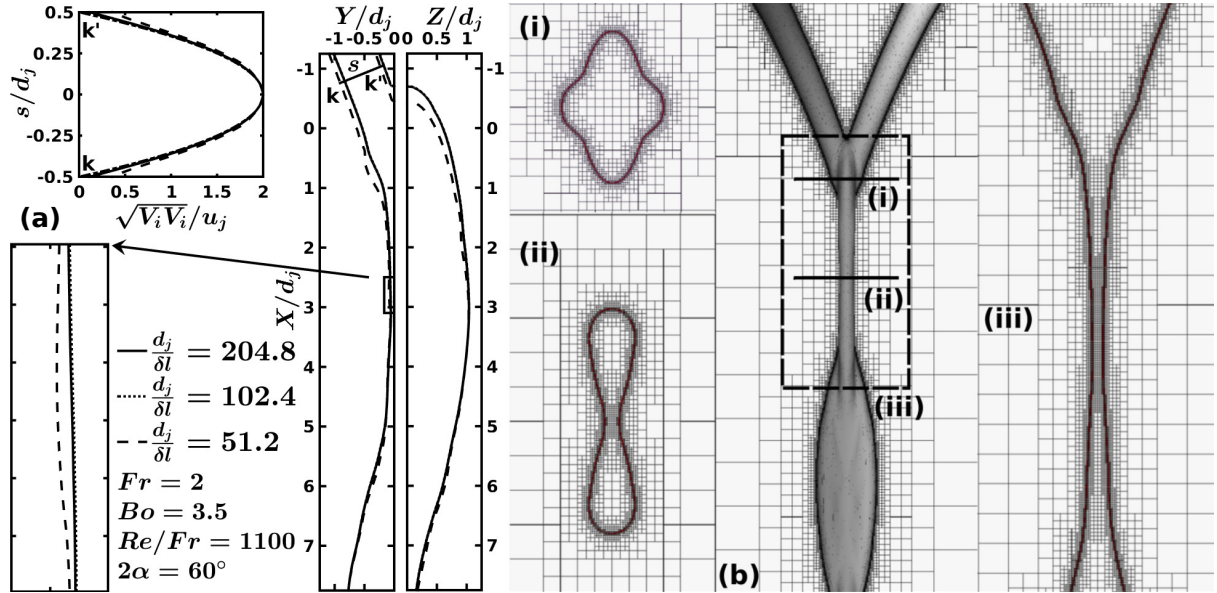


FIGURE 2.1: (a) Mesh sensitivity analysis for a representative chain structure with the outer periphery and velocity profile near the inlet and (b) representation of the Adaptive Mesh Refinement (AMR) technique at critical locations.

(Chen et al., 2013). To obtain good liquid film resolution,  $\delta l$  is varied to match the above-mentioned criteria. In one representative simulation, we show the effect of variation of  $\delta l$ , in figure 2.1 (a), on the sheet profile and velocity pattern of the jet. It can be observed that at  $\frac{d_j}{\delta l} = 102.4$ , well resolved film is obtained with acceptable computational cost ( $\sim 50\%$  less than  $\frac{d_j}{\delta l} = 204.8$ ). The results from this mesh sensitivity result have been summarized in table 2.1. Mesh structure around different critical parts of the chain is shown in figure 2.1(b) which establishes sufficiency of grid points even inside smallest thickness of the film. In the next section, the validation of the employed numerical method is demonstrated.

## 2.4 Validation of the numerical model

To check the accuracy of the developed mesh structure, results from simulations are compared with experimental observations obtained by Bush and Hasha, 2004. Figure 2.2 presents a description of the results in this test. The one-to-one correspondence between the experimental sheet profile (Bush and Hasha, 2004) and the numerical results is reported in figure 2.2(a). Making use of the fact that their experiments led to supercritical (greater than capillary wave speed) sheet speeds, Bush and Hasha, 2004 were able to construct the variation of liquid volume flux ( $Q(\theta) = \frac{dQ}{d\theta} = uhr$ ) inside the sheet by scanning across the sheet and collecting liquid through a fine opening. In order to get quantitative

TABLE 2.1: Performance data of the processors used for simulations to determine the refinement level in the Grid Independence Study. The simulations are done using four Intel Core i7-6500U CPU having clock speed of 2.5GHz each and 8 GB RAM.

$\left(\frac{d_j}{\delta l}\right)_{max}$	$\left(\frac{t_{CPU}}{t_{actual}}\right)$ (days/s)
51.2	$\sim 20$
102.4	$\sim 28$
204.8	$\sim 60$

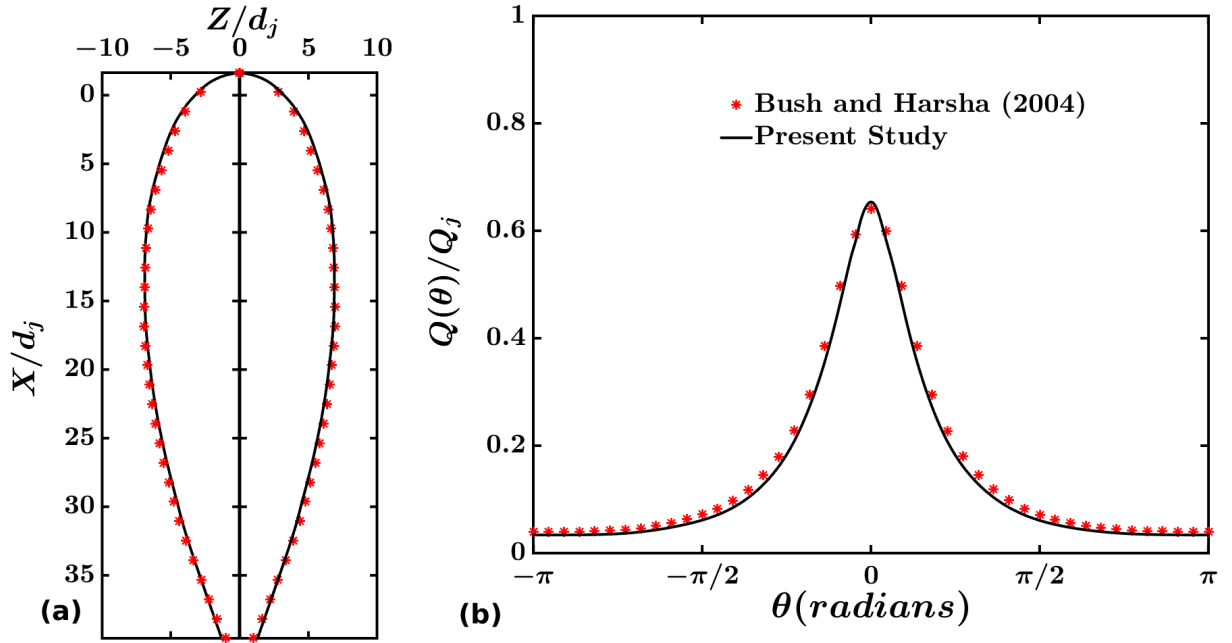


FIGURE 2.2: Illustration of the validation of numerical model undertaken by comparison of (a) numerical interface and (b) liquid flux variation with the azimuthal angle,  $\theta$ . The numerically obtained results are superimposed with the respective experimental values obtained by Bush and Hasha, 2004.

validation, the variation of liquid volume flux ( $Q(\theta)$ ) inside the sheet is also plotted in figure 2.2(b) along with Bush and Hasha, 2004. Matching between present numerical simulations and pioneering experimental result by Bush and Hasha, 2004 provides confidence for the numerical understanding of the phenomenon, in our work. In the next chapter, results of the numerical simulation using the presented model to study the collision of liquid jets are summarized.

## **Chapter 3**

### **Collision of liquid jets**

### 3.1 Collision and Sheet formation

As the laminar liquid jets collide, a thin sheet bounded by thicker rims is formed in the median plane, perpendicular to the axes of the jets. The initialization of the liquid jets is done using small inclined cylinders with circular cross-section as shown in equation 3.1.

$$\frac{|(\mathbf{x} - \mathbf{x}_1) \times (\mathbf{x} - \mathbf{x}_2)|}{|\mathbf{x}_2 - \mathbf{x}_1|} = \frac{d_j}{2} \quad (3.1)$$

Here,  $\mathbf{x}$  is the loci of the cylinder with axis marked by the vector  $\mathbf{x}_2 - \mathbf{x}_1$  and  $d_j$  is the diameter of the cylinder. Across this inclined cylinder, a parabolic velocity profile is patched as discussed in section 2.3. In this section, the formation of chain structure due to the collision of liquid jets is discussed and the temporal variation of the phenomena is illustrated. This is followed by the study of the kinematics of fluid parcels inside the liquid sheet. At last, the three-dimensional streamline structure is discussed.

#### 3.1.1 The process of chain formation

Figure 3.1 shows temporal evolution of the fluid sheet when the two jets (shown in figure 3.1(a)) collide. The reference for temporal variations is kept at the instant when the jets collide. The fluid parcels are dispatched radially outwards from the point of impingement. In case of the head on collision of the liquid jets ( $\alpha = 90^\circ$ ), the sheet formed is always radial in the absence of gravity (Eggers and Villermaux, 2008) and the point of stagnation is in-line with the two liquid jets (Inamura and Shirota, 2014). However, in this case the net inertia of jets and gravity result in a bay leaf like sheet as shown in figures 3.1(b) and 3.1(c). Present zone of consideration lies in  $0.5 < Fr < 4$ , where gravity plays a major role unlike Bremond and Villermaux, 2006; Bush and Hasha, 2004. In absence of surface tension or at very high Weber number, the sheet keeps on expanding (figures 3.1(d) and 3.1(e)), leading to the formation of the open rim structures (Chen et al., 2013; Taylor, 1960). However, due to the action of the surface tension, the sheet stops expanding and the two rims are formed at the periphery because of the accumulation of the fluid parcels from the liquid sheet. Surface tension also provides the necessary centripetal acceleration to sustain the liquid rims. These rims undergo a second oblique collision (figure 3.1(f)) at an angle smaller than the initial collision (figure 3.1(b)). After the secondary impingement, similar to figure 3.1(c), a flow biased sheet begins to develop (figure 3.1(g)). Formation of this second link has no effect on the characteristics features of the primary link as the sheet speed is supercritical (Bush and Hasha, 2004), and therefore can be independently studied.

Temporal advancement results in the formation of a full-fledged secondary link as shown in figures 3.1(h) to 3.1(j). It must be noted that the plane of formation of this sheet is orthogonal to that of the primary link and therefore the secondary link shares the same plane as the axes of the jets. The process continues and a series of mutually orthogonal links are obtained, successively reducing in size until a long single liquid jet is formed (Bush and Hasha, 2004). After the initial transients, as seen from figure 3.1 and its inset, the links become steady (non-dimensionalized time,  $T \left( \frac{u_j t}{d_j} \right) = 8.5$  as representation in primary link), which has been analyzed further.

#### 3.1.2 Velocity variation inside the sheet

Jets progress towards each other and collide at a point in the median sheet plane to form a sheet bounded by leaf-like rims. Fast moving, the thin sheet possess radial velocity pattern emerging from a stagnation point,  $\delta_\pi$  higher than the impingement location. Inamura and Shirota, 2014 have established  $\delta_\pi = \lambda d_j / (2 \sin \alpha)$ , where the factor  $\lambda$  is a function of the impingement angle. It needs to be noted that  $\delta_\pi$  changes its value, depending upon the angle of impingement and can be taken as a parameter. Considering  $\delta_\pi$  and velocity vectors obtained from numerical simulations for two sets of non-dimensional numbers, flow pattern inside the sheet is reported in figure 3.2(a). It can be observed that velocity vectors follow a self-similar smooth path, as traced by sheet boundary. An increase of sheet span can be also

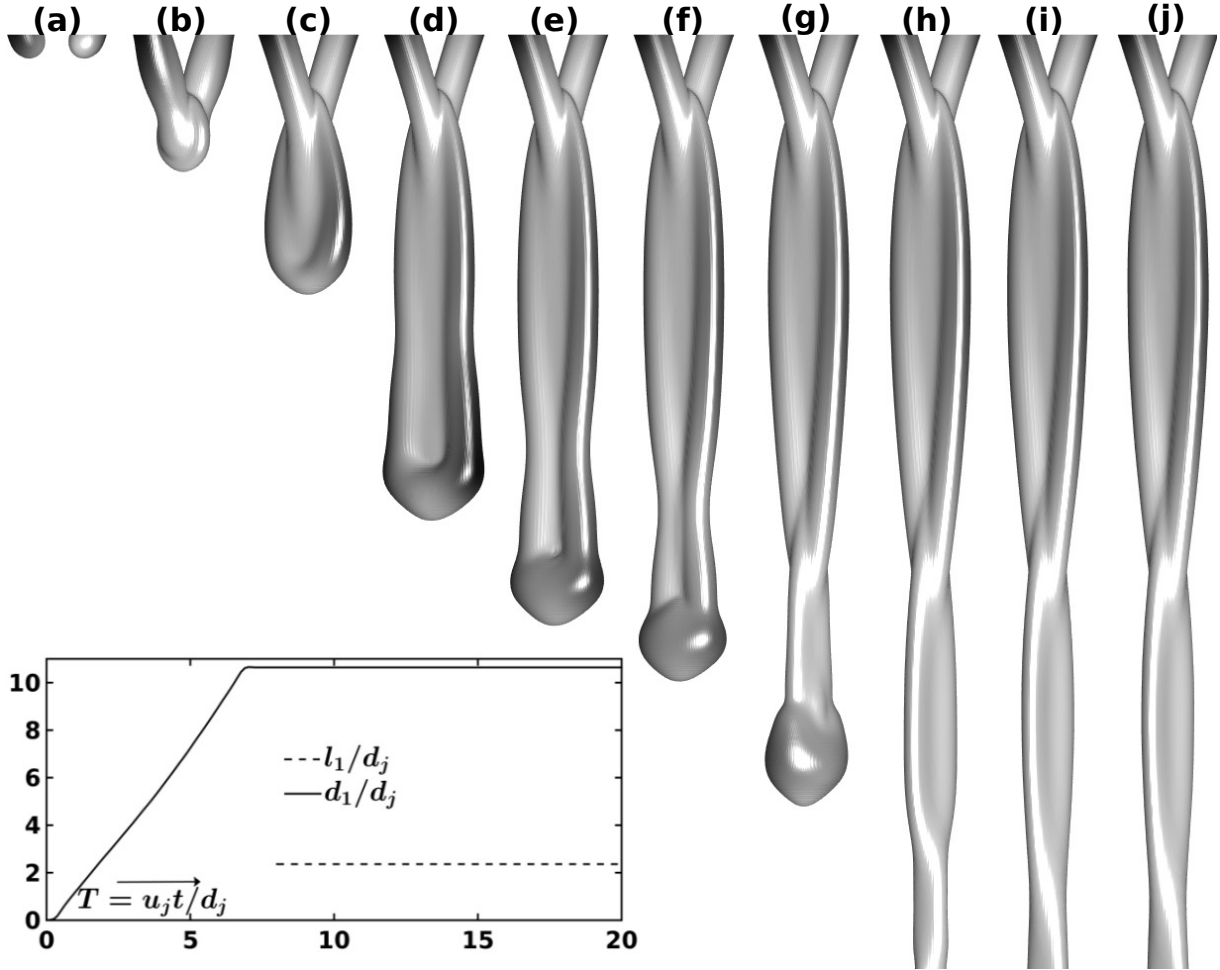


FIGURE 3.1: Formation of the liquid chain due to the collision of laminar jets. The figure illustrates the transient period through the temporal advancement from (a) pre-collision symmetric jets to  $T(\frac{u_j t}{d_j}) =$  (b) 1.5, (c) 4, (d) 5, (e) 5.5, (f) 6.5, (g) 8.5, (h) 14.5, (i) 18.5 and (j) 20. The variation of  $d_1$  and  $l_1$  with time is shown in inset ( $\alpha, Fr, Re/Fr, Bo = 30^\circ, 2.5, 34, 5$ ). The video for this figure is added as a supplementary material.

noticed from the figure for a higher velocity of impacting jets.

An effort has been made to observe the local sheet velocity ( $u_f(r, \theta)$ ) at a given radial and azimuthal point. The local sheet velocity ( $u_f(r, \theta)$ ) was first used by Choo and Kang, 2002 and denotes the steady average flow across the thickness of the sheet. Moreover, figure 3.2(a) shows the presence of both radial and azimuthal components of the velocity vectors. Therefore, the local sheet velocity ( $u_f(r, \theta)$ ) can be expressed as equation 3.2, where  $Y$  is the coordinate direction parallel to link's thickness.

$$u_f(r, \theta) = \int_0^1 \sqrt{V_i V_i} d(Y/h) \quad (3.2)$$

$V_i$  denotes the velocity field in Cartesian-tensor notation and  $\sqrt{V_i V_i}$  is the total magnitude of the velocity given by  $\sqrt{V_r^2 + V_\theta^2 + V_z^2}$ . Azimuthal and radial velocities are considered here to accommodate spread of fluid streams, forming chain and subsequent links in orthogonal planes. The variation of the local sheet velocity ( $u_f(r, \theta)$ ) along radial plane at different azimuthal angles have been shown in figure 3.2(b). It can be observed that the order of change in the fluid velocity across the radial distance from the point of impact is less than the change across the azimuthal direction (also discussed by Choo and Kang, 2002). Making use of this feature, the sheet velocity ( $u_s(\theta)$ ) in a particular azimuthal direction has been also

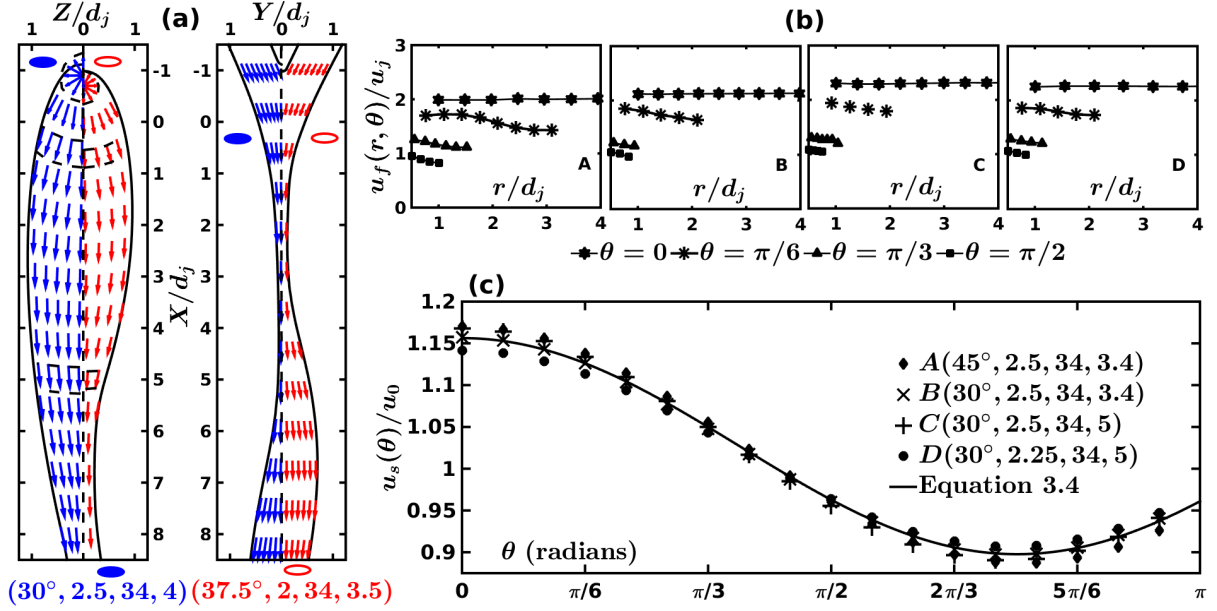


FIGURE 3.2: Flow kinematics of the fluid parcels: (a) velocity vector field for two representative cases, (b) variation of velocity in the radial direction for four representative cases and (c) their radially averaged sheet velocity ( $u_s(\theta)$ ), non-dimensionalized with the average sheet velocity ( $u_0$ ) along the azimuthal direction. The parameters identifying the identity of the cases follow ( $\alpha$ ,  $Fr$ ,  $Re/Fr$ ,  $Bo$ ).

obtained by integrating the local sheet velocity  $u_f(r, \theta)$  as given by equation 3.3. This sheet velocity ( $u_s(\theta)$ ) gives a measure of the velocity of dispatch of fluid parcel in a given azimuthal direction.

$$u_s(\theta) = \int_0^1 u_f(r, \theta) d\left(\frac{r}{r_{max}(\theta)}\right) \quad (3.3)$$

It must be noted that  $r_{max}(\theta)$  is the maximum radial spread of the liquid sheet in a particular azimuthal direction ( $\theta$ ). Upon non-dimensionalization of sheet velocity with its average ( $u_0 = \int_0^\pi u_s(\theta) d\theta$ ), a self-similar behavior in azimuthal direction is observed for a wide diversity of non-dimensional parameters reported in figure 3.2(c). In this figure, four arbitrarily chosen parameters are shown which adhere to a functional relationship of  $u_s(\theta)$  in the following fashion:

$$\frac{u_s(\theta)}{u_0} = 1.03 + 0.13 \cos\left(\frac{4.18\theta}{\pi}\right) \quad (3.4)$$

It needs to be noted that the equation 3.4 is valid for a large range of non-dimensional numbers explored in the present study, forming stable chain structure ( $0^\circ < \alpha \leq 45^\circ$ ,  $Fr \sim 1$ ,  $Bo \sim 1$  and  $10 \leq Re \leq 2300$ ). Using figure 3.2 and equation 3.4, it can be realized that the thickness-averaged velocity field in equation 3.2 is a function of only one coordinate  $X$  and the functional dependence on coordinates  $r$ ,  $\theta$  is only through their combination  $X = r \cos \theta$ . Further, the integration in equation 3.3 over the radial direction is equivalent to the integral of function of local sheet velocity ( $u_f$ ) over the interval  $X \in \{0, r_{max}(\theta) \cos \theta\}$ . The resulting function of sheet velocity will then be implicitly dependent on the azimuthal direction. Moreover, equation 3.4 clearly demonstrates that the non-dimensional sheet velocity ( $\frac{u_s(\theta)}{u_0}$ ) differs from unity (as predicted by Choo and Kang, 2002). The sheet velocity ( $u_s(\theta)$ ) not only represents the kinematics of the flow field inside the link but also acts as a transition parameter. The chain structure no longer remains stable because of Kelvin - Helmholtz instability if  $u_s$  exceeds a limit (Villermaux and Clanet, 2002). The discussion so far gives an idea about the two-dimensional velocity field. Next we discuss the three dimensional velocity field with an aid of streamlines and vectors at different locations to explain the subsequent collisions.

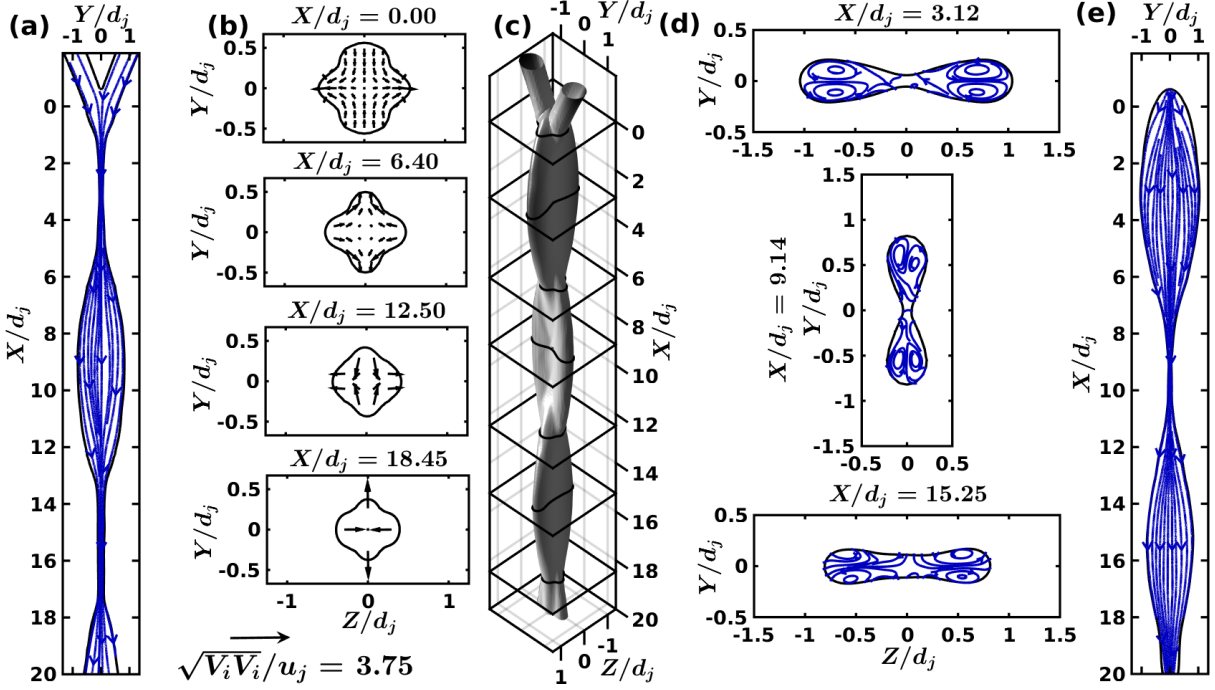


FIGURE 3.3: Three dimensional velocity field for  $(\alpha, Fr, Re/Fr, Bo) = (30^\circ, 2, 1125, 3.4)$  with (a) XY plane streamlines, (b) velocity vector field in the YZ plane at different collision locations, (c) the three dimensional stable chain structure, (d) streamlines at maximum link widths in the YZ plane and (e) XZ plane streamlines.

### 3.1.3 Three dimensional streamline structure

An overall consideration of the three-dimensional chain structure (figure 3.3(c)) allows us to obtain velocity patterns at different axial locations. The streamlines follow steadily the phase contour boundary, with those inside the chain structure going in trajectories similar to the outer boundary as shown in figures 3.3(a) and 3.3(e). Figure 3.3(b) puts an effort towards highlighting velocity vectors at primary, secondary and tertiary links. One can observe from figure 3.3(b) that the spread of liquid influence at collision planes is reducing continuously as  $X/d_j$  increases. At the primary ( $X/d_j = 0$ ) and tertiary ( $X/d_j = 12.5$ ) collision points, the liquid jets and rims respectively converge onto themselves ( $Z/d_j = 0$ ) marked by retracting velocity field, whereas the liquid sheet grows ( $Y/d_j = 0$ ) in the Z direction, marked by an expanding velocity field. Trends opposite to these are obtained at the secondary ( $X/d_j = 6.40$ ) and quaternary ( $X/d_j = 18.45$ ) collision planes where a retracting velocity field is present at  $Y/d_j = 0$  and expansion happens at  $Z/d_j = 0$ . This leads to the formation of three visible orthogonal links in this case (figure 3.3(c)). The velocity vector magnitudes go on increasing at each subsequent collision planes as the gravitational head is converted to dynamic head leading to narrowing of the extent of liquid phase boundary in the XZ plane. In the primary link, this converging-diverging trend of velocity vectors is continued from above the first collision point ( $X/d_j = 0$ ) to the plane where the extent of the link perpendicular to the net flow direction in the plane of the link is maximum ( $X/d_j = 3.12$ ). As illustrated in figure 3.3(d), the streamlines at the location of maximum width imply that the component of velocity perpendicular to the liquid sheet phase boundary is zero ( $\frac{d\Psi}{dn} = 0$ ). This results in the formation of distinguished circulation patterns inside the lobes at the locations of the maximum extent ( $X/d_j = 3.12, 9.14$  and  $15.25$ ) corresponding to the three links visible in this case. Reduction of collision strength at different planes explains diminishing spans of the links, which can be also seen from sheet cross-sectional images (figure 3.3(d)).

A characteristic twist can be found in streamlines (figure 3.4) as the flow propagates downstream through the locations of subsequent collisions. The twist occurs as the fluid parcels are restricted by surface tension to follow the chain's outer periphery. This twist is characterized by the offset of these streamlines

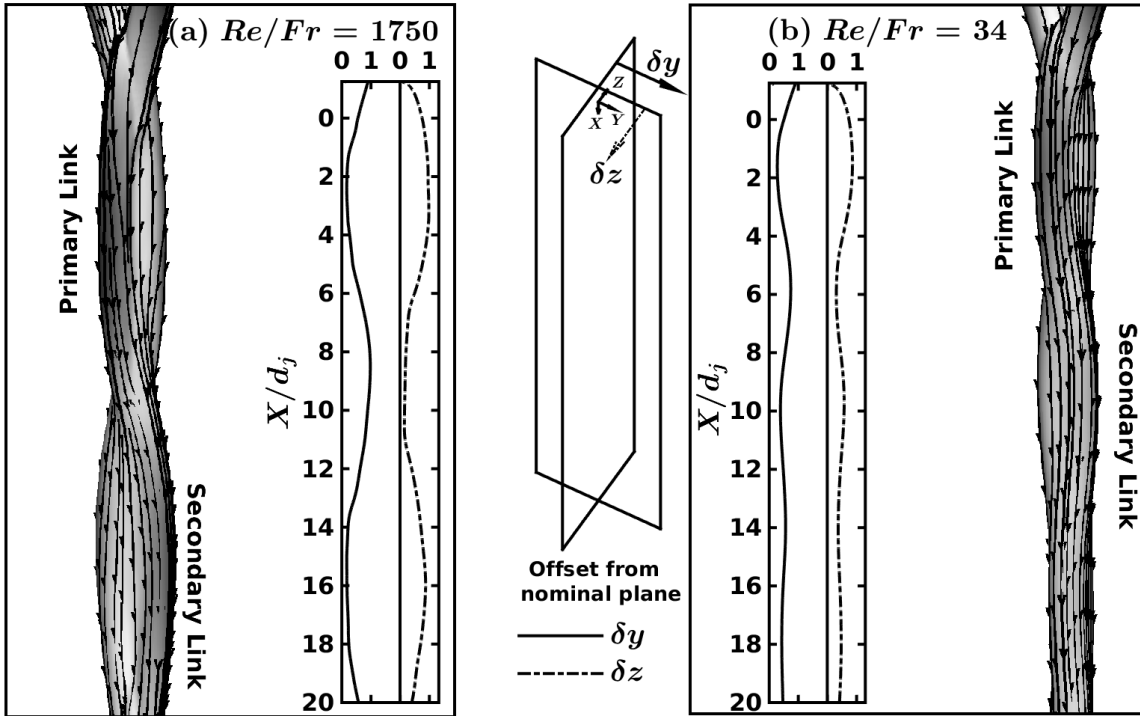


FIGURE 3.4: Three dimensional streamlines embedded on the chain structure illustrating the twist incurred as they traverse through the region of subsequent collisions for  $\alpha = 30^\circ$ ,  $Fr = 2$ ,  $Bo = 3.4$  and (a)  $Re/Fr = 1750$  and (b)  $Re/Fr = 34$ . The figures in inset show the offset ( $\delta y$  from XZ plane and  $\delta z$  from XY plane) of the streamline at the extreme end of the chain structure as it moves downstream with the flow for the corresponding cases.

from the two mutually orthogonal planes: the XY plane containing the axes of the liquid jets ( $\delta z$ ) and the XZ median plane orthogonal to this one ( $\delta y$ ). The offset of the most extreme streamline are shown in the inset of figure 3.4 for two representative cases having different ratios of Reynolds Number and Froude Number ( $Re/Fr = 1750$  in figure 3.4(a) and  $Re/Fr = 34$  in 3.4(b)). The offset of all the streamlines from the XZ plane ( $\delta y$ ) decreases continuously as the liquid jets approach each other (retracting velocity field as shown in figure 3.3(b)). After the collision, two extreme streamlines in XZ and XY planes are depicted in the inset of figures 3.4 (a) and 3.4 (b). It is observed that  $\delta y$  decreases continuously through the first link, but downstream of the second collision, the offset starts to increase, reaching the maxima at the location of the maximum width of the secondary link. The opposite trend is observed for the XY plane whereby the offset ( $\delta z$ ) increases after the first collision continuously till the maximum width of the primary link and then decreases for the secondary link. These variations in the offset in streamlines show the presence of twist, which is prominent until viscous effects start dominating and only a single jet of liquid is left at the end of the chain structure (as shown in figure 3.4(b) beyond  $X/d_j = 16$ ). These viscous forces lead to dissipation of energy as the liquids jets (or rims for the post-primary link) collide with each other. It is clear from our discussions above that values of dimensionless numbers  $\alpha$ ,  $Fr$ ,  $Bo$  and  $Re/Fr$  determine the three-dimensional stable chain structures. The next section is devoted to analyzing such effects.

### 3.2 Parametric Variation

Formation of the liquid sheet bounded by the rims is governed by inertia, viscous, buoyancy and surface forces apart from the angle of impingement between the jets ( $\alpha$ ). The relative importance of these forces is described by the parameters  $Fr$ ,  $Bo$  and  $Re/Fr$ , as mentioned above. In this section, critical assessment of chain shapes is made for various non-dimensional numbers and impingement angles. Yang

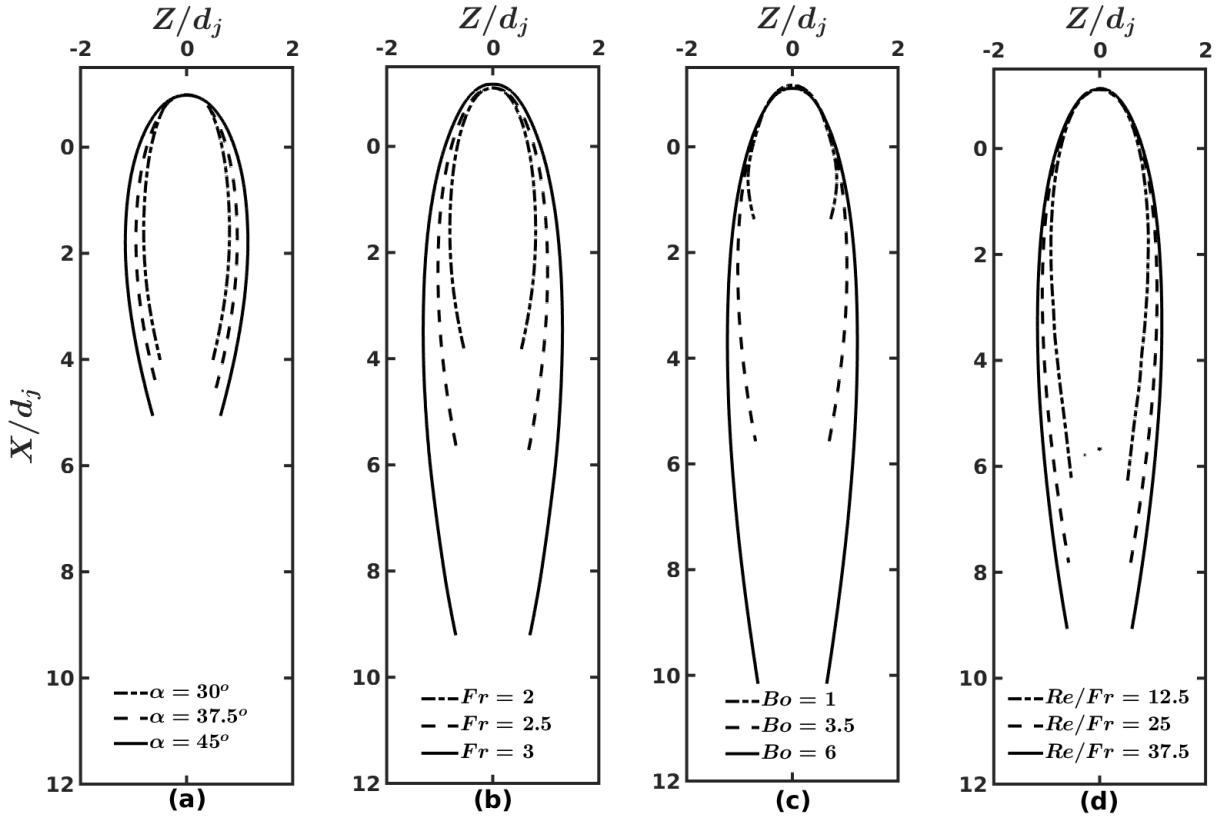


FIGURE 3.5: Variation of first link boundary with (a)  $\alpha$  at  $Fr = 2.5$ ,  $Bo = 4.57$  and  $Re/Fr = 34$  (b)  $Fr$  at  $\alpha = 30^\circ$ ,  $Bo = 3.4$  and  $Re/Fr = 34$  (c)  $Bo$  at  $\alpha = 30^\circ$ ,  $Fr = 2.5$  and  $Re/Fr = 34$  and (d)  $Re/Fr$  at  $\alpha = 30^\circ$ ,  $Fr = 2$  and  $Bo = 3.4$ .

et al., 2014 acknowledged the importance of these parameters on collision process and formation of the first link. This analysis is used to generalize the effects of these parameters on the dimensions of first link to the entire chain structure. The study is followed by the development of a regression model for the prediction of the shape and size of the first link using the control parameters of the liquid jets.

### 3.2.1 Variation of control parameters

Figure 3.5 shows the effects of the variation of the non-dimensional parameters on the first link which can be generalized in figure 3.6 for the entire chain structure. Figures 3.6(a)- 3.6(d) show numerical chain structure for a several sets of parameters  $\alpha$ ,  $Fr$ ,  $Bo$  and  $Re/Fr$ . An increase in impingement angle leads to decrease of jet momentum in direction of gravity ( $u_j \cos \alpha$ ). Further, it must be noted that the sheet dimension in the direction parallel to that of gravity is dominated by the loss in gravitational potential (Taylor, 1960), which remains unaffected during the transition. Further, the jet momentum in the plane perpendicular to the gravity is increased ( $u_j \sin \alpha$ ). These effects result in a substantial increase in width of the sheet, keeping the length more or less intact (figures 3.5(a) and 3.6(a)). Alternatively, as the jet momentum is increased (increase in  $Fr$ ), the resulting links are bigger (figures 3.5(b) and 3.6(b)) due to the fluid inertia. The increment can be explained with the fact that the increase in  $Fr$  or jets' momenta is directed related to the increase in the strength of the jets which in turn is a measure of the expansion tendency of the liquid sheets (Yang et al., 2014). One can clearly see this effect is transmitted to the subsequent links as well. Further, the surface tension is a crucial entity which influences the expansion of the link. As the surface tension is decreased ( $Bo$  increased), the link can expand until inertial and centrifugal forces balance it. This justifies obtaining larger links for higher values of  $Bo$  as seen in figures 3.5(c) and 3.6(c). As the surface tension is increased (low  $Bo$  regime), the system tries to go towards the minimum surface energy decreasing the dimensions of the corresponding links (link in figure 3.6(c))

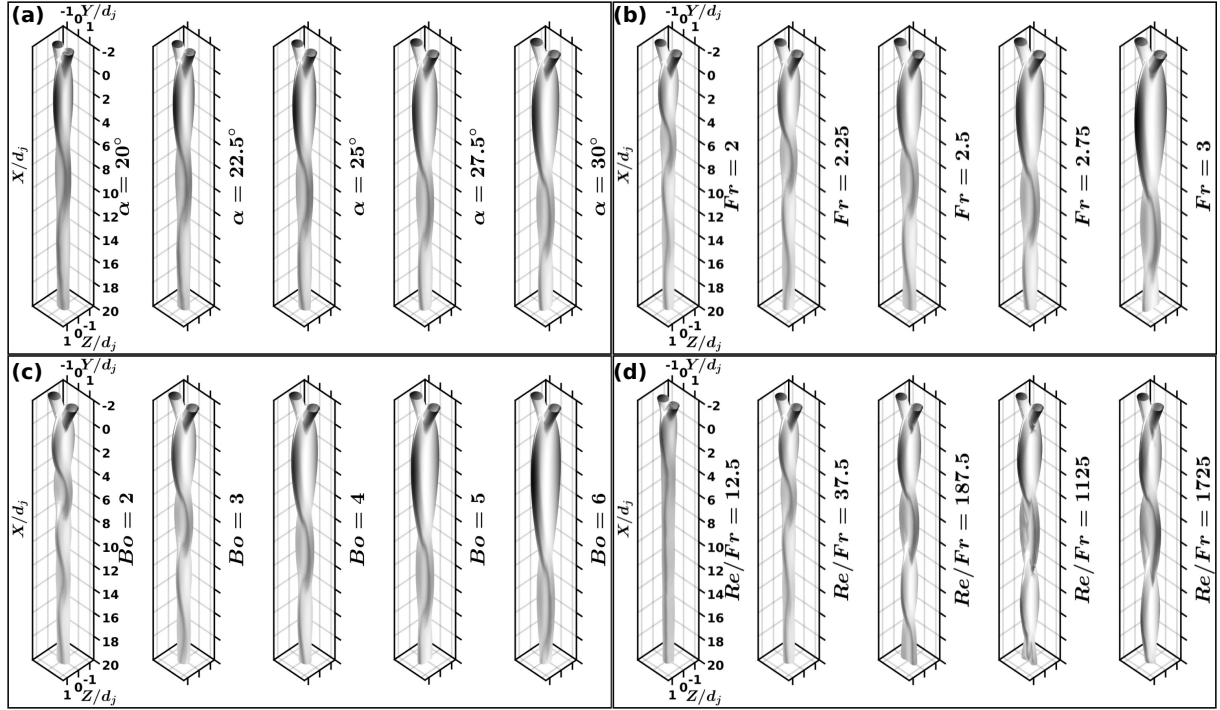


FIGURE 3.6: High fidelity numerical simulations of liquid jets collision to form chain structure for variation of (a)  $\alpha$  at  $Fr = 2.5$ ,  $Bo = 4.57$  and  $Re/Fr = 34$  (b)  $Fr$  at  $\alpha = 30^\circ$ ,  $Bo = 3.4$  and  $Re/Fr = 34$  (c)  $Bo$  at  $\alpha = 30^\circ$ ,  $Fr = 2.5$  and  $Re/Fr = 34$  and (d)  $Re/Fr$  at  $\alpha = 30^\circ$ ,  $Fr = 2$  and  $Bo = 3.4$ .

from  $Bo = 6$  to 2). Further, the collision of cylindrical jets and rims is also observed to be influenced by viscous dissipations. Decreasing the viscosity (increasing  $Re/Fr$ ) leads to considerable increase in sheet dimensions but its effect saturates at lower ranges of liquid viscosities (figures 3.5(d) and 3.6(d)). This can be easily illustrated by observing the change in sheet dimension from  $Re/Fr = 12.5$  to  $Re/Fr = 37.5$  as compared to the change from  $Re/Fr = 187.5$  to  $Re/Fr = 1725$ . Effect of change in liquid viscosity dies down as inertia and surface tension overshadow its resistance to form similar shape and sizes of links. It can also be noticed that it is the viscous dissipations that result in the decrement in the size of subsequent links leading to a point where the sheet coalesces into a single jet of fluid. The effect is prominent in figure 3.6(d) for  $Re/Fr = 12.5$ .

### 3.2.2 Prediction of chain structure using regression analysis

Considering  $\Delta Z$  is the rim to rim distance at a particular vertical location ( $X$ ) of the symmetric sheet, a third order polynomial is used to fit ( $R^2 > 0.975$ ;  $SSE < 0.01$ ) the sheet shape for various influencing parameters. The functional form of the polynomial is as follows:

$$\frac{\Delta Z}{2d_j} = \sum_{n=0}^{n=3} p_n \left( \frac{X}{d_j} \right)^n \quad (3.5)$$

Efforts are also made to relate polynomial coefficients ( $p_n$ ) with non-dimensional numbers using linear regression analysis. Hence,  $p_n$  can be expressed as

$$p_n = C_{0,n} (\sin \alpha)^{C_{1,n}} (Fr)^{C_{2,n}} (Bo)^{C_{3,n}} (Re)^{C_{4,n}} \quad (3.6)$$

Values of  $C_{m,n}$  ( $\forall m \in 0, 4$ ) in equation 3.6 are tabulated in the table 3.1 obeying  $R^2$  norm of regression higher than 0.925. Predictability of the correlation with numerical chain contours are shown in the insets

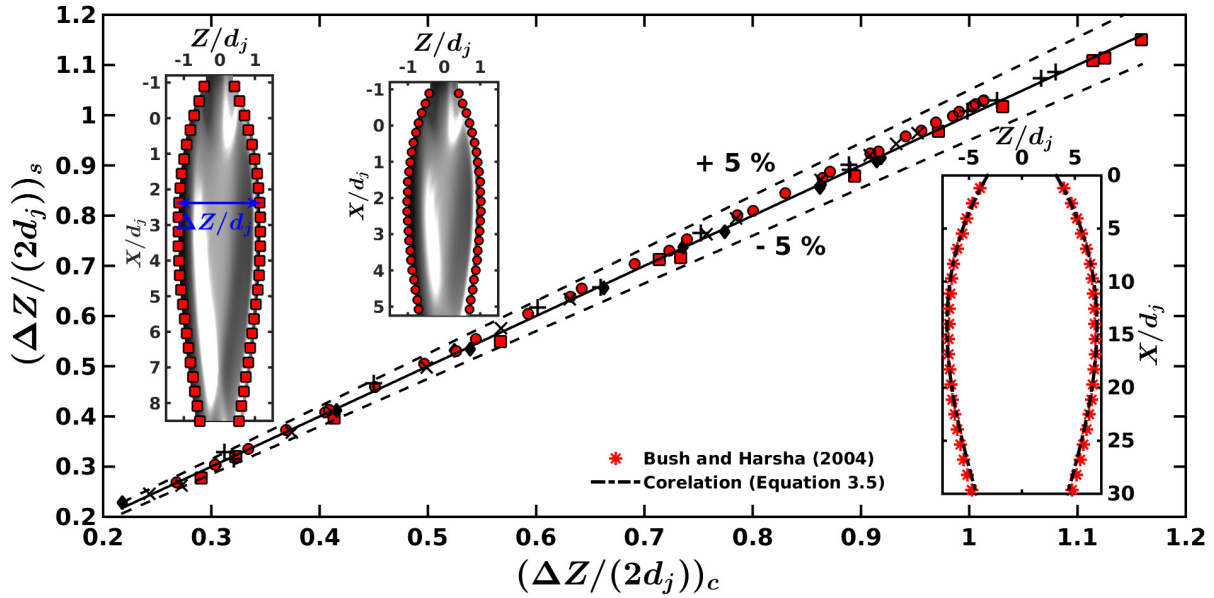


FIGURE 3.7: Comparison between the values of expansion of the sheet outer periphery ( $\Delta Z(x)$ ) as predicted from equation 3.5 and from numerical simulations for different test cases with (symbol,  $\alpha$ ,  $Fr$ ,  $Bo$ ,  $Re/Fr$ ) = ( $\blacksquare$ ,  $30^\circ$ , 2.5, 5, 34); (+,  $30^\circ$ , 2.5, 4, 34); ( $\blacklozenge$ ,  $30^\circ$ , 2.5, 2.3, 20); ( $\times$ ,  $25^\circ$ , 2.5, 4.57, 34) and ( $\bullet$ ,  $30^\circ$ , 2.5, 3.75, 20). The first two inset figures (from the left) visualize the corresponding three dimensional structure of the first link for the primary link and the third inset depicts the comparison between the equation 3.5 and the results of Bush and Hasha, 2004.

TABLE 3.1: Factors ( $C_{m,n}$ ) involved in equation 3.6 determined by linear regression analysis to find the polynomial coefficients of equation 3.5.

$C_{m,n}$	n				
	0	1	2	3	
m	0	3.662	2.720	0.353	0.512
	1	-0.082	0.490	1.146	0.592
	2	-2.166	-0.940	0.408	0.761
	3	-1.504	-0.831	0.074	-0.065
	4	-0.657	-0.290	0.029	0.039

of figure 3.7 for two different cases of non-dimensional numbers. It can be also observed from figure 3.7 that the developed correlation gives a very good match ( $\pm 5\%$ ) with the numerical sheet profiles. So as to check the capability of the correlation, for prediction of experimental profiles of the chain structure, the comparison is made between observation of Bush and Hasha, 2004 and equation 3.5. The reported excellent match in the inset of figure 3.7 confirms the universality of the developed correlation. It is essential to understand the formation physics of widely influenced sheet structure generated due to the collision of jets. Next section dedicatedly discusses the issue.

### 3.3 Analytical Model

To bring out the physical insights of the liquid jet collision, idealizations are made for tracing back the sheet profile as a result of the collision between a train of fluid quanta (each of mass  $m$ ), analogous to jet, in the plane of the sheet. It is assumed that the fluid quantum in a given jet interacts only with its mirror image in the other jet and that they are non-deformable. The collision is taken as friction-less. However, the follow-up trajectory of these fluid parcels after the collision is considered damped so as

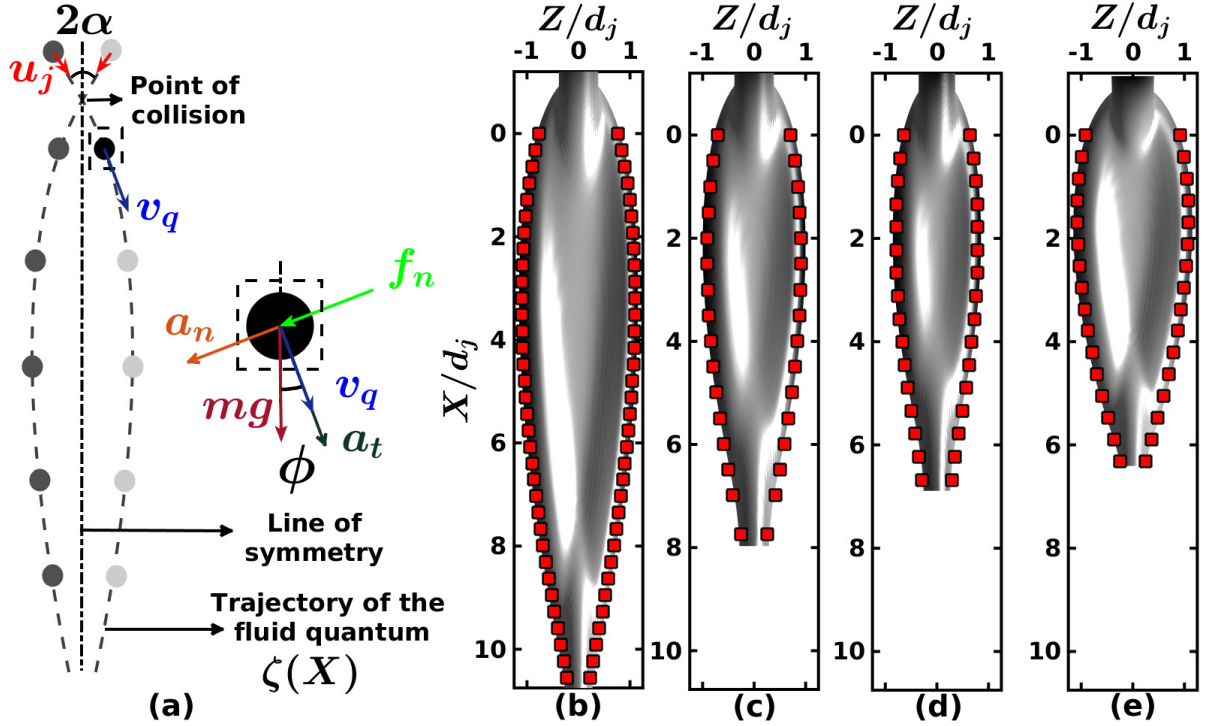


FIGURE 3.8: Fluid quanta collision analogy: (a) schematic of the model and free-body diagram and comparison between the link shape obtained through numerical simulations and the fluid quantum trajectory ( $\zeta$ , ■) for  $(\alpha, Fr, Re/Fr, Bo) =$  (a)  $(30^\circ, 2.5, 34, 5)$ , (b)  $(30^\circ, 2.5, 23, 3.85)$ , (d)  $(30^\circ, 2, 34, 4.56)$  and (e)  $(45^\circ, 2, 34, 3.4)$ .

to mimic resistive forces like viscous and surface tension. A free body diagram and schematic of the fluid quanta collision assumption to replicate the sheet structure is depicted in figure 3.8(a). Apart from inertial and gravitational forces, on the fluid particle, a damping force of magnitude  $f_n$  (to impose the effect of viscous dissipation and surface forces) is also attached in the direction perpendicular to the individual packet's instantaneous velocity, post-collision. Absence of these resistive forces will make infinitely stretched sheet (Taylor, 1960), with  $f_n = 0$  case. In-situ assessment of damping force based on local velocity may improve the prediction of resistive forces which has not been targeted in the present effort. Reference frame for the trajectory of the fluid quantum ( $\zeta$ ) is considered to have the origin at the point of collision with  $\zeta = 0$  at  $X = 0$ . Free body force analysis of the fluid particle, post-collision can be expressed as equations 3.7a and 3.7b, with accelerations  $a_n$  and  $a_t$  in normal ( $n$ ) and tangential ( $t$ ) directions respectively.

$$\text{Direction t: } a_t = v_q \frac{dv_q}{ds} = g \cos \phi \quad (3.7a)$$

$$\text{Direction n: } a_n = g \sin \phi + \frac{f_n}{m} = \frac{v_q^2}{r_c} \quad (3.7b)$$

Here,  $r_c$  is the radius of curvature in  $\zeta-X$  plane and  $\phi = \tan^{-1} \left( \frac{d\zeta}{dX} \right)$ . Integrating tangential momentum equation with increment  $ds = dX / \cos \phi$  along with boundary condition at  $X = 0$ , instantaneous fluid particle velocity ( $v_q$ ) can be obtained as  $\sqrt{u_j^2 + 2gX}$ . Rearrangement of momentum equation in the normal direction after defining  $\Lambda$  as  $\frac{f_n}{mg}$  and inertial length scale,  $\chi$  equivalent to  $\frac{u_j^2}{2g}$ , one obtains:

$$r_c (\sin \phi + \Lambda) = 2\chi \left( \frac{X}{\chi} + 1 \right) \quad (3.8)$$

After necessary integration, equation 3.8 simplifies to:

$$\sin \phi = \sin \alpha + (\Lambda + \sin \alpha) \left( \frac{1}{\sqrt{\frac{X}{x} + 1}} - 1 \right) \quad (3.9)$$

Recalling that  $\tan \phi = \frac{d\zeta}{dX}$  and expressing  $\Lambda / \sin \alpha = \eta$ , profile of fluid quantum movement can be characterized as:

$$\frac{d\zeta}{dX} = \tan \left\{ \sin^{-1} \left[ \sin \phi_0 (1 + \eta) \left( \frac{1}{\sqrt{\frac{X}{x} + 1}} - 1 \right) \right] \right\} \quad (3.10)$$

The functional form of the fluid particle trajectory, the equivalence of sheet profile, can be integrated numerically to obtain the coordinate points in the  $\zeta - X$  plane after tuning only control factor,  $\eta$  from some simulated profiles. In this process,  $L^1$  relative error norm is kept below 10%. Efforts have been also made to express control parameter,  $\eta$  in terms of non-dimensional numbers for the range of values presented in this work. With 99%  $R^2$  regression norm,  $\eta$  can be related with non-dimensional numbers as:

$$\eta = 3.28(\sin \alpha)^{-0.077}(Fr)^{0.502}(Bo)^{-0.248}(Re)^{-0.084} \quad (3.11)$$

Proposed concept of collision of fluid quanta for mimicking the sheet profile is also tested with phase contours of numerical simulations. Some representative matches are shown in figures 3.8(b) - 3.8(e) in connection of primary link. Fundamental analysis of forces, a single controlling parameter in sheet profile (equation 3.10) and an excellent match with numerical data supplies in-depth knowledge about the formation of the liquid chain. Next, we focus on the mutual relationship between links formed at successive orthogonal planes.

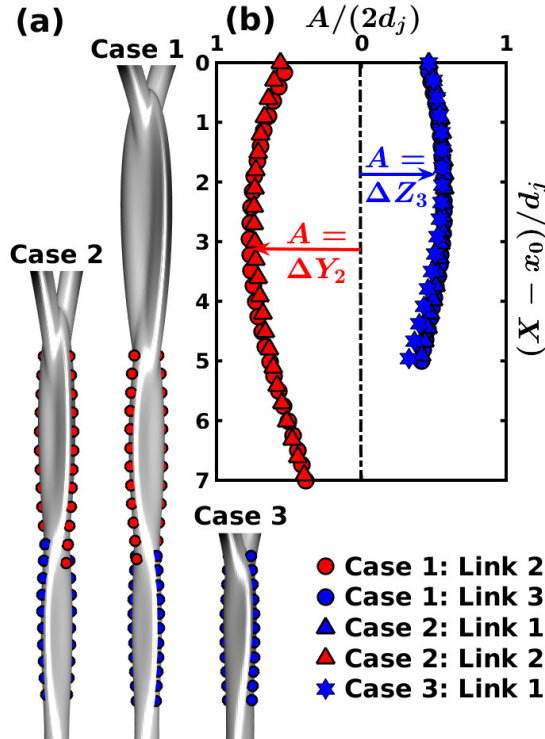


FIGURE 3.9: Inter-relation between links of chain reproduction of secondary link of Case 1 ( $\alpha = 30^\circ$ ,  $Fr = 2.5$ ,  $Bo = 4$ ,  $Re/Fr = 34$ ) as primary link of case 2 ( $\alpha = 25^\circ$ ,  $Fr = 2.2$ ,  $Bo = 4$ ,  $Re/Fr = 34$ ) and tertiary link of Case 1 as secondary link of Case 2 and primary link of case 3 ( $\alpha = 11.25^\circ$ ,  $Fr = 1.98$ ,  $Bo = 4$ ,  $Re/Fr = 34$ ) using (a) three dimensional chain structure and (b) two dimensional planar link locations.

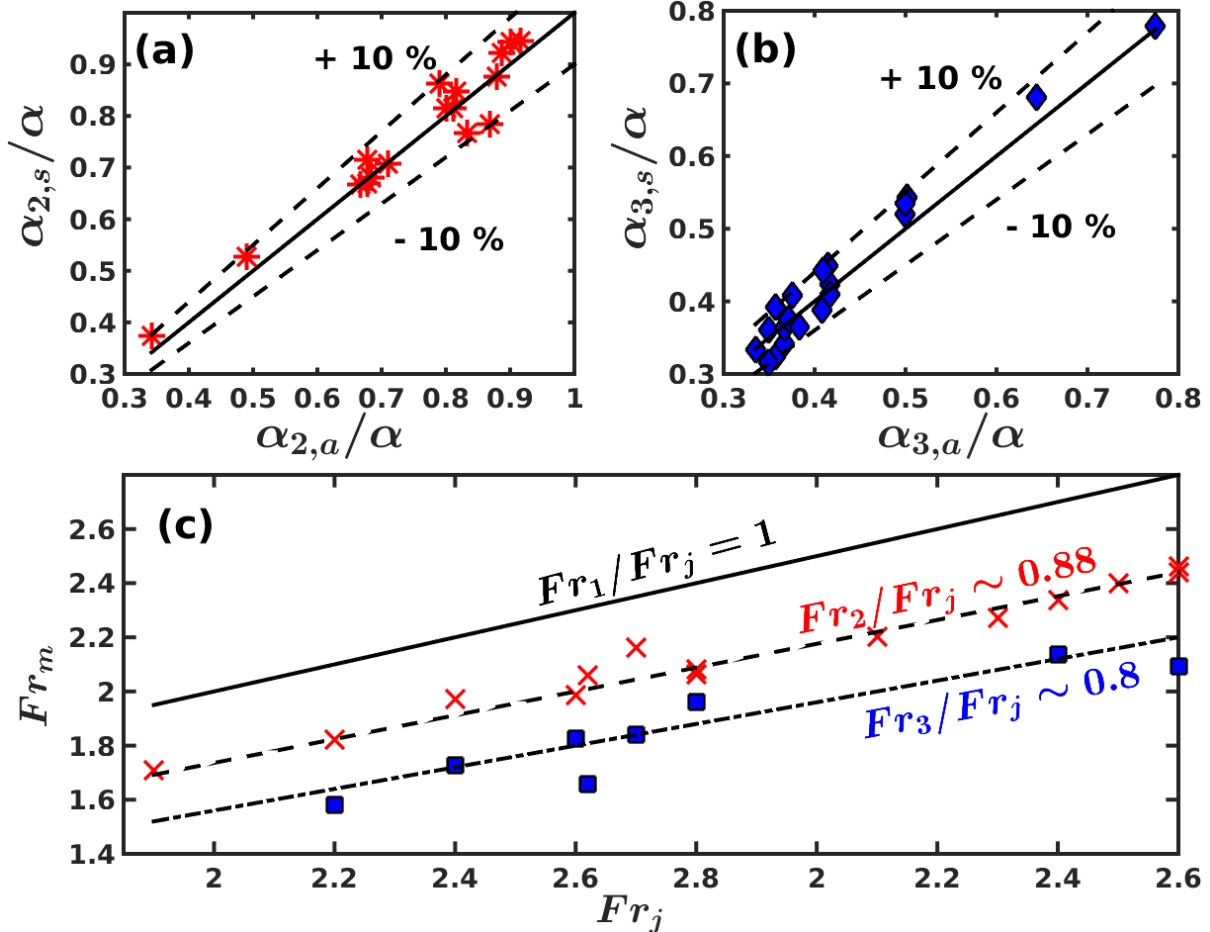


FIGURE 3.10: Generalization of fluid rim collision for the higher order links with the prediction of angles of impingement for (a) secondary and (b) tertiary collisions and (c) the account of rim strength ( $Fr$ ) in different links.

### 3.4 Inter-relation between inter-connected links

The secondary and tertiary links observed in mutually perpendicular planes initiate with the collision of rims in preceding links. From our numerous simulations in the wide range of operating parameters, it can be observed that secondary, tertiary and subsequent links of a chain are equivalent to primary, secondary and subsequent links of another chain having different operating parameters. Hence, it is proposed that subsequent links are equivalent to resultant of collision between two free jets having reduced strength. To prove our assumption, for example in figure 3.9(a), a representative chain structure is identified for  $\alpha = 30^\circ$ ,  $Fr = 2.5$ ,  $Bo = 4$ ,  $Re/Fr = 34$  (Case 1), in which secondary links showed resemblance with primary link of  $\alpha = 25^\circ$ ,  $Fr = 2.2$ ,  $Bo = 4$ ,  $Re/Fr = 34$  (Case 2). Continuing this one can also establish analogy among tertiary link of Case 1, secondary link of Case 2 and primary link of  $\alpha = 11.25^\circ$ ,  $Fr = 1.98$ ,  $Bo = 4$ ,  $Re/Fr = 34$  (Case 3). One to one correspondence of these links of different cases establishing present proposal is shown in the comparative graph of figure 3.9(b).

It can be commented that subsequent links are reduced in size, giving a feeling of resultant of impact between two weaker jets. The analogy between interconnected links in a chain and one level lower link of another chain is found to be valid with  $\pm 10\%$  confidence for the entire region of search space of the operating parameters ( $\alpha$ ,  $Fr$ ,  $Re/Fr$ ,  $Bo$ ). A critical assessment of links in chain structure and rim profile has also established that angle of impingement between rims successively reduces  $\alpha_n/\alpha_{n-1} < 1 \forall n = 1, 2, 3$  and higher integers. It has been also checked that analogy of collision between fluid parcels and formation of the link by the interaction between rims is also valid after taking

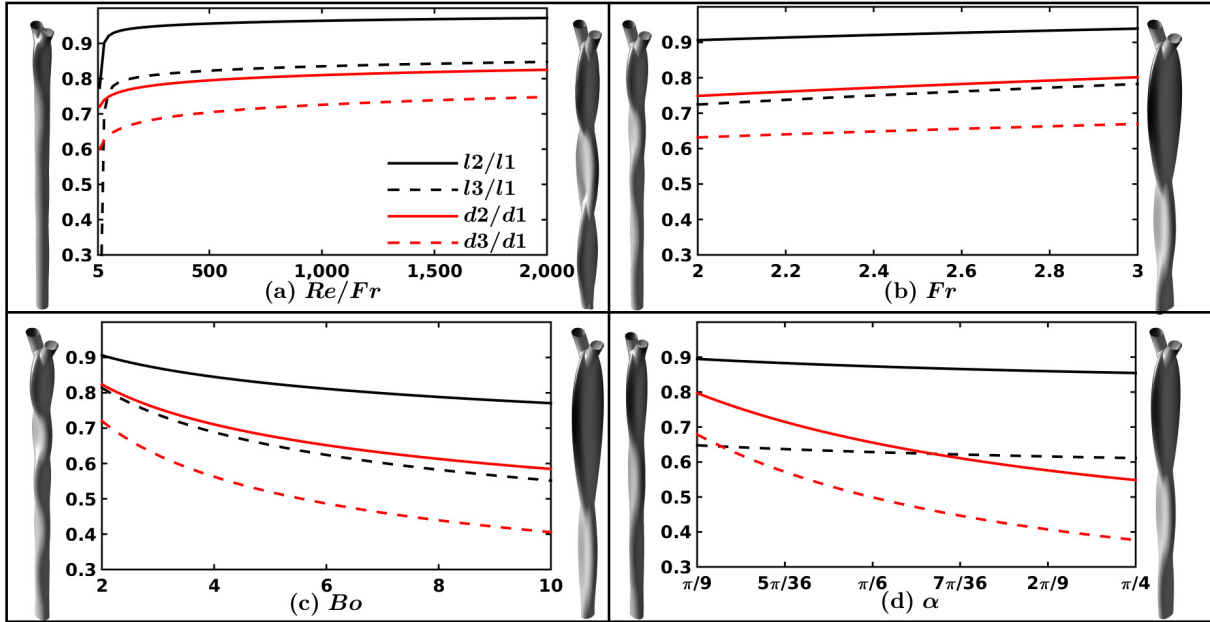


FIGURE 3.11: Evaluation of the dimensional characteristics of the secondary and tertiary links relative to the primary link, for variations of (a)  $\alpha$  at  $Fr = 2.5$ ,  $Bo = 4.57$  and  $Re/Fr = 34$  (b)  $Fr$  at  $\alpha = 30^\circ$ ,  $Bo = 3.4$  and  $Re/Fr = 34$  (c)  $Bo$  at  $\alpha = 30^\circ$ ,  $Fr = 2.5$  and  $Re/Fr = 34$  and (d)  $Re/Fr$  at  $\alpha = 30^\circ$ ,  $Fr = 2$  and  $Bo = 3.4$ .

the reduction of angle of impingement into consideration. This trend is shown in the figures 3.10(a) - 3.10(b) for secondary and tertiary links for few chain cases randomly scattered in search space. With only  $\pm 10\%$  error, theory of collision between the fluid quanta (equations 3.10 - 3.11) has also found to be applicable for  $n^{th}$  order link of chain. Polynomial proposed in equation 3.5 also predicts formation of  $n^{th}$  order link satisfactorily with modified strength and impingement angle. Clustering of points near (1,1) for secondary link (figure 3.10(a)) and (0,0) for tertiary link (figure 3.10(b)) establishes continuous reduction of impingement angle  $\alpha_n$  with increase in link number  $n$ . Besides the reduction in angle of impingements, the interaction between rims of a link can be also considered as the collision between jets of lesser Froude number ( $Fr_m$ ) than  $Fr_j$ . The monotonous decrement of  $Fr_m$  is observed as one traverses in subsequent higher level links along a chain. Figure 3.10(c) establishes this idea where the ratio between rim Froude number of secondary link ( $Fr_2$ ) to jet Froude number ( $Fr_j$ ) has been fitted as 0.88 and that of same for the tertiary link ( $Fr_3/Fr_j$ ) as 0.8.

These decrements are a result of the viscous dissipations which are prominent at the time of the collision and has been illustrated in figure 3.11 (with the extreme cases of variations shown as insets figures across each graph) for the entire domain of non-dimensional numbers considered in the present work. The dimensional characteristics of the secondary and tertiary links are studied as relative to the primary link. The range of values of  $l_i/l_1$  and  $d_i/d_1$  is always less than 1. Further, it must be noted that the final resultant liquid jet formed after the diminishing of chain structure also shows some undulations on its surface. Therefore, we have considered the presence of higher order links only if the difference in relative dimensional characteristics is more than 30%. For fluids with higher viscosities, the formation of this resultant jet is most prominent as shown in figure 3.11(a). As the viscosity is decreased ( $Re$  is increased), there is a sudden increase in the dimensional characteristics because of the reduced viscous dissipations at the time of collision of subsequent rims of the sheet. However, similar to the effects of  $Re$  on single link dimensions, this influence saturates after the initial increase as for the less viscous fluids (high  $Re$ ), the formation of chain structure is surface tension and inertia driven. Further, with an increase in the inertia of the liquid jets, the individual links grow in size but because of the viscous dissipations, this effect is not transmitted equally downstream of the flow. The second link also increases in dimensions but the length and width of the second link are always smaller than the primary link (figure 3.11(b)). Moreover,

an increase in the  $Bo$  (decrement in the surface tension coefficient of the interface), the length and width of the first link increase substantially (Bremond and Villermaux, 2006; Yang et al., 2014). As a result, the primary sheet thickness and the rim diameter decrease leading to the reduction of the inertia of the rims responsible for the secondary and subsequent collisions. Therefore, the dimensional characteristics of the higher order links as compared to the first one decreases with an increase in  $Bo$  (figure 3.11(c)). A similar decrement is also observed if the angle of impingement is increased (figure 3.11(d)) as the primary link grows faster in size than the others. Though the idea of the interrelation between the links is established only for first three, it can be extrapolated for higher order elements in the chain until it transforms into a jet.

## **Chapter 4**

# **Conclusion and Future Work**

## 4.1 Conclusion

The stable chain structures are formed by the collision of laminar liquid jets when the inertia forces are, in order of magnitude, similar to the surface tension forces. A series of fully resolved detailed numerical simulations are performed to get the following conclusions:

- The individual links, formed by collision of cylindrical jets (primary) or rims (secondary onward), occupy mutually orthogonal planes with a successive reduction in size owing to viscous effects.
- The variation of the velocity field across the radial coordinate is found to be negligible whereas the azimuthal variation of the sheet velocity is scaled using its average, given by an empiric relation. At the collision planes, the velocity field is found to be retracting in the direction of the colliding jets and rims whereas it is expanding in the plane of the formed sheets.
- The inertial and gravitational forces provide a measure of the expansion of these sheets counteracted by the surface tension at the interface and viscous dissipations at the subsequent collisions. An increase in the impingement angle ( $\alpha$ ) leads to wider links of the chain with a negligible change in the length of individual links. Intuitively, the size of the stable chain structure increases with an increase in the momenta of the jets ( $Fr$ ) or with a decrease in the strength of the surface tension force (increasing  $Bo$ ). Increase in the  $Re$  presents a sharp increase in the dimensions of the chain, which saturates at the higher values of  $Re$ .
- The individual symmetric sheet profile can be modeled using a third order polynomial, with an accuracy of  $\pm 5\%$ , with coefficients dependent on various non-dimensional numbers featuring the interplay of different forces.
- The analytical model is developed by considering the fundamental forces of gravity and surface tension lead to formulation of the sheet profile using only one free parameter which has been empirically related to the flow parameters.
- Higher order links are found to be similar to lower or primary level element formed due to impact between jets of reduced  $Fr$  and  $\alpha$ .

## 4.2 Future Work

- Study of bubble entrainment by impingement of liquid jets into a pool surface and subsequent interactions between the clusters.
- Study of collision of liquid jets with high Reynolds number.

TABLE 4.1: Work Plan

Objectives	May - July 2017	August - October 2017	November 2017 - January 2018	February - April 2018
Formation of fluid chain by collision of liquid jets				
Interaction by impingement of liquid jets into a pool				
Collision of liquid jets at high Reynolds number				

# ACHIEVEMENTS TILL DATE

- Sanjay, V.** and Das, A. K. (2017). “Formation of liquid chain by collision of two laminar jets”. *Physics of Fluids, Impact Factor = 2.232*, 29.11, p. 112101. DOI: [10.1063/1.4998288](https://doi.org/10.1063/1.4998288).
- Sanjay, V** and Das, A. K. (2017). “On air entrainment in a water pool by impingement of a jet”. *AICHE Journal, Impact Factor = 2.836*, 63.11, pp. 5169–5181. ISSN: 1547-5905. DOI: [10.1002/aic.15828](https://doi.org/10.1002/aic.15828).
- Soni, A., **Sanjay, V**, and Das, A. K. (2017). “Consequences of interaction between asymmetric liquid jets”. In: *Paper ID: 64, 44th National Conference on Fluid Mechanics and Fluid Power*.
- Jain, A., **Sanjay, V**, and Das, A. K. (2017a). “Asymmetry in air entrainment inside liquid pool due to impingement of an inclined jet”. In: *Paper ID: IHMTC2017-13-0828; 24th National and 2nd International ISHMT-ASTFE Heat and Mass Transfer Conference*.
- Jain, A., **Sanjay, V**, and Das, A. K. (2017b). “Interaction of bubble clusters formed due to adjacent impingement of liquid jets in a pool”. In: *Paper ID: 68, 44th National Conference on Fluid Mechanics and Fluid Power*.
- Sanjay, V** and Das, A. K. (2016). “On the gas-liquid entrainment by impingement of liquid jet onto a pool”. In: *Reference #50, 9th International Conference on Multiphase Flow*.
- Aggarwal, A., **Sanjay, V**, Kumar, P., and Das, A. K. (2016). “Generation of a liquid sheet by an oblique impingement of interacting jets: a numerical investigation”. In: *Paper ID: 267, Proceedings of CHEMCON*.
- Sanjay, V** and Das, A. K. (2015). “Bubble life cycle during entrainment by Jet impingment in liquid pool”. In: *ID FM-052, Proceedings of CHEMCON*.

# REFERENCES

- Bell, J. B., Colella, P., and Glaz, H. M. (1989). “A second-order projection method for the incompressible Navier-Stokes equations”. *Journal of Computational Physics* 85.2, pp. 257–283.
- Bremond, N. and Villermaux, E. (2006). “Atomization by jet impact”. *Journal of Fluid Mechanics* 549, pp. 273–306.
- Bush, J. W. M. and Hasha, A. E. (2004). “On the collision of laminar jets: fluid chains and fishbones”. *Journal of Fluid Mechanics* 511, pp. 285–310.
- Chen, X., Ma, D., Yang, V., and Popinet, S. (2013). “High-fidelity simulations of impinging jet atomization”. *Atomization and Sprays* 23.12.
- Choo, Y. J. and Kang, B. S. (2001). “Parametric study on impinging-jet liquid sheet thickness distribution using an interferometric method”. *Experiments in Fluids* 31.1, pp. 56–62.
- Choo, Y. J. and Kang, B. S. (2002). “The velocity distribution of the liquid sheet formed by two low-speed impinging jets”. *Physics of Fluids* 14.2, pp. 622–627.
- Choo, Y. J. and Kang, B. S. (2007). “The effect of jet velocity profile on the characteristics of thickness and velocity of the liquid sheet formed by two impinging jets”. *Physics of Fluids* 19.11, p. 112101.
- Chorin, A. J. (1968). “Numerical solution of the Navier-Stokes equations”. *Mathematics of Computation* 22.104, pp. 745–762.
- Clanet, Christophe and Villermaux, Emmanuel (2002). “Life of a smooth liquid sheet”. *Journal of fluid mechanics* 462, pp. 307–340.
- Da, F., Hahn, D., Batty, C., Wojtan, C., and Grinspun, E. (2016). “Surface-only liquids”. *ACM Transactions on Graphics (TOG)* 35.4, p. 78.
- Da Vinci, Leonardo (1508). “The Notebooks of Leonardo da Vinci”. *Trans: E MacCurdy, (New York: George Brazillier)*, p. 756.
- Eggers, J. and Villermaux, E. (2008). “Physics of liquid jets”. *Reports on Progress in Physics* 71.3, p. 036601.
- Ekimova, M., Quevedo, W., Faubel, M., Wernet, P., and Nibbering, E. T. J. (2015). “A liquid flatjet system for solution phase soft-x-ray spectroscopy”. *Structural Dynamics* 2.5, p. 054301.
- Erni, P. and Elabbadi, A. (2013). “Free impinging jet microreactors: controlling reactive flows via surface tension and fluid viscoelasticity”. *Langmuir* 29.25, pp. 7812–7824.
- Hasson, D. and Peck, R. E. (1964). “Thickness distribution in a sheet formed by impinging jets”. *AICHE Journal* 10.5, pp. 752–754.
- Ibrahim, E. A. and Przekwas, A. J. (1991). “Impinging jets atomization”. *Physics of Fluids A: Fluid Dynamics* 3.12, pp. 2981–2987.
- Inamura, T. and Shirota, M. (2014). “Effect of velocity profile of impinging jets on sheet characteristics formed by impingement of two round liquid jets”. *International Journal of Multiphase Flow* 60, pp. 149–160.
- Inoue, C., Watanabe, T., and Himeno, T. (2008). “Study on atomization process of liquid sheet formed by impinging jets”. In: *44th AIAA/ASME/SAE/ASEE Joint Propulsion Conference & Exhibit*, p. 4847.
- Inoue, C., Watanabe, T., and Himeno, T. (2009). “Liquid sheet dynamics and primary breakup characteristics at impingement type injector”. In: *45th AIAA/ASME/SAE/ASEE Joint Propulsion Conference & Exhibit*, p. 5041.

- Kumar, Parmod, Das, Arup Kumar, and Mitra, Sushanta K (2016). “Physical understanding of gas-liquid annular flow and its transition to dispersed droplets”. *Physics of Fluids* 28.7, p. 072101.
- Kumar, Parmod, Das, Arup K, and Mitra, Sushanta K (2017a). “Air entrainment driven by a converging rotational field in a viscous liquid”. *Physics of Fluids* 29.10, p. 102104.
- Kumar, Parmod, Das, Arup K, and Mitra, Sushanta K (2017b). “Bending and growth of entrained air filament under converging and asymmetric rotational fields”. *Physics of Fluids* 29.2, p. 022101.
- Lhuissier, Henri and Villermaux, Emmanuel (2011). “The destabilization of an initially thick liquid sheet edge”. *Physics of Fluids* 23.9, p. 091705.
- Ling, Y., Zaleski, S., and Scardovelli, R. (2015). “Multiscale simulation of atomization with small droplets represented by a Lagrangian point-particle model”. *International Journal of Multiphase Flow* 76, pp. 122–143.
- Popinet, S. (2003). “Gerris: a tree-based adaptive solver for the incompressible Euler equations in complex geometries”. *Journal of Computational Physics* 190.2, pp. 572–600.
- Popinet, S. (2009). “An accurate adaptive solver for surface-tension-driven interfacial flows”. *Journal of Computational Physics* 228.16, pp. 5838–5866.
- Rayleigh, Lord (1879). “On the capillary phenomena of jets”. *Proceedings of the Royal Society of London* 29.196-199, pp. 71–97.
- Rayleigh, Lord (1889). “On the tension of recently formed liquid surfaces”. *Proceedings of the Royal Society of London* 47.286-291, pp. 281–287.
- Shen, Y. B. and Poulikakos, D. (1998). “Thickness variation of a liquid sheet formed by two impinging jets using holographic interferometry”. *ASME Journal of Fluids Engineering* 120.3, pp. 482–487.
- Taylor, G. (1960). “Formation of thin flat sheets of water”. *Proceedings of the Royal Society of London A: Mathematical, Physical and Engineering Sciences* 259.1296, pp. 1–17.
- Villermaux, E. and Clanet, C. (2002). “Life of a flapping liquid sheet”. *Journal of Fluid Mechanics* 462, pp. 341–363.
- Wadhwa, N., Vlachos, P., and Jung, S. (2013). “Noncoalescence in the oblique collision of fluid jets”. *Physical review letters* 110.12, p. 124502.
- Yang, L.-J., Zhao, F., Fu, Q.-F., and K.-D.Cui (2014). “Liquid sheet formed by impingement of two viscous jets”. *Journal of Propulsion and Power* 30.4, pp. 1016–1026.